

A powerful lidar system capable of one-hour measurements of water vapour in the troposphere and the lower stratosphere as well as the temperature in the upper stratosphere and mesosphere

Lisa Klanner¹, Katharina Höveler¹, Dina Khordakova², Matthias Perfahl¹, Christian Rolf², Thomas Trickl¹, Hannes Vogelmann¹

¹Karlsruher Institut für Technologie, Institut für Meteorologien und Klimaforschung (IMK-IFU), Kreuzeckbahnstr. 19, D-82467 Garmisch-Partenkirchen, Germany

²Forschungszentrum Jülich, IEK-7, Wilhelm-Johnen-Straße, 52425 Jülich, Germany

Correspondence to: Dr. Thomas Trickl, e mail: thomas@trickl.de, Tel. 0049-8821-50283

Abstract. A high-power Raman lidar system has been installed at the high-altitude research station Schneefernerhaus (Garmisch-Partenkirchen, Germany) at 2675 m a.s.l., at the side of an existing wide-range differential-absorption lidar (DIAL). An industrial XeCl laser was modified for linearly polarized single-line operation at an average power of about 180 W. This high power and a 1.5-m-diameter receiver allow us to extend the operating range for water-vapour sounding to 20 km for a measurement time of just one hour, at an uncertainty level of the mixing ratio of 1 to 2 ppm. This was achieved for a vertical resolution varied between just 0.2 and 0.6 km in the stratosphere. The lidar was successfully validated with a balloon-borne cryogenic frost-point hygrometer (CFH). In addition, temperature measurements to altitudes around 87 km were demonstrated for one hour of signal averaging. The system has been calibrated with the DIAL, the CFH and radiosondes.

Key words: Lidar, Raman lidar, water vapour, temperature

1 Introduction

Water vapour in the upper troposphere and lower stratosphere (UTLS) is the key factor controlling how much thermal infrared radiation escapes from the atmosphere into space (e.g., Kiehl and Trenberth, 1997; Schmidt et al., 2010; Lacis et al., 2013). In a warmer climate the atmosphere takes up more water vapour from the sea surface. However, this increase could be counteracted by additional cloud formation and precipitation. Also vertical exchange processes could change in a warmer climate (Trickl et al., 2010a; 2020a). Water vapour trends in the troposphere derived from observations are discussed in literature. Paltridge et al. (2009) report negative trends for the period 1973 to 2007 at all free-tropospheric altitudes in NCEP (National Centers for Environmental Prediction, <https://www.ncep.noaa.gov/>) re-analysis data, in particular in the upper troposphere, in contrast to the expectations from climate modelling. Other studies show at least regionally positive trends (Ross and Elliott, 2001; Mieruch et al. 2008; Chen and Liu, 2016). However, they evaluate columnar quantities that are dominated by the moist boundary layer where thermal radiation is trapped by water vapour anyway. In the lower stratosphere, the Boulder series shows a trend reversal from positive to negative occurred around 2000 (Hurst et al., 2011), but the pronounced positive trend during the early phase since the late 1980s is not confirmed for other locations (Solomon et al., 2010; Hegglin et al., 2014).

Due to the role of water vapour as the most important greenhouse gas the optimization of high-accuracy, range-resolved vertical sounding instrumentation covering the entire free troposphere and the lower stratosphere has

1 become more and more important during the past two decades (Kämpfer et al., 2013). All the most commonly
2 used sensors used for routine measurements have limitations. Operational radiosondes have been greatly
3 improved within the troposphere in recent years, but deficiencies exist in the very cold tropopause region and the
4 lower stratosphere where the sensors exhibit slow response and low sensitivity (Miloshevich et al., 2006; Vömel
5 et al., 2007a; Steinbrecht et al., 2008; Kämpfer et al., 2013). Balloon-borne cryogenic frost-point hygrometers
6 (CFH; Vömel et al., 2007b; 2016; Kämpfer et al., 2013; Hurst et al., 2016) and Lyman alpha hygrometers (Kley
7 and Stone, 1978; Weinstock et al. 1990; Khattatov et al., 1994; Hintsä et al., 1999; Zöger et al., 1999; Kämpfer
8 et al., 2013), though being highly accurate, are rarely used in dense routine measurement programmes due to
9 their elevated costs. Ground-based microwave radiometers have an excellent temporal coverage, but their
10 application is limited to the lower and middle troposphere (Westwater, 1978; Han and Westwater, 1995; Solheim
11 and Godwin, 1998) and altitudes above 20 km (Nedoluha et al., 1997; Deuber et al., 2004; 2005; Kämpfer et al.,
12 2013) with somewhat limited vertical resolution. The value of satellite-borne measurements (Kämpfer et al.,
13 2013) is limited by the considerable spatial averaging that results in a loss of information due to the high
14 variability of water vapour even in the lower stratosphere (Zahn et al. 2014), but can yield reasonable averages
15 and global coverage (e.g., Solomon et al., 2010).

16 There is just one long quantitative ground-based sounding series of stratospheric water vapour, obtained with the
17 Boulder balloon-borne CFH (Scherer et al., 2008; Hurst et al., 2011). These measurements have been carried out
18 since 1980 at intervals of about one measurement per month. Because of the considerable variability of water
19 vapour up to at least the UTLS more frequent measurements with good vertical resolution are desirable (Müller
20 et al., 2016). This variability is caused to a major extent by transport-induced patterns. Injections of water
21 vapour into the stratosphere occur not only in the tropics (Rosenlof, 2003), where also freeze-drying has been
22 claimed to matter (see, e.g., the discussions by Peter et al. (2003), Luo et al. (2003), Jensen et al. (2007) and
23 Zahn et al. (2014)), but also in the jet-stream regions (Stohl et al., 2003; and references therein). Warm conveyor
24 belts (WCBs) can lift moist polluted air from the boundary layer to the tropopause region (Stohl and Trickl,
25 1999). Overshooting WCBs even transfer water vapour into the lower stratosphere (LS; Stohl, 2001), although
26 possibly diminished by dehydration due to cirrus-cloud formation (cirrus clouds being almost ubiquitous in
27 WCB air probed by our lidar systems). Most investigations related to this topic have been limited to airborne
28 measurements of the chemical composition of the tropopause region (e.g., Pan et al., 2007; Gettelman et al.,
29 2011; Zahn et al., 2014). It is reasonable to assume that water vapour transported into the LS by TST is an
30 important target for vertical sounding of H₂O with enhanced temporal density. The opposite mechanism,
31 stratosphere-to-troposphere transport (STT), is much more important than previously thought, at least in Central
32 Europe after some increase over several decades (Trickl et al., 2010a; 2020a). Growing STT can contribute to a
33 lowering of the tropospheric humidity.

34 Lidar-based measurements have the potential of good temporal and vertical resolution and are, therefore,
35 attractive for resolving transport-related concentration changes. However, the use of lidar systems for water
36 vapour implies a major challenge due the strong decrease of both the backscatter signal and the water-vapour
37 concentration with altitude. Despite the problems related to the extreme signal dynamics the NDACC (Network
38 for the Detection of Atmospheric Composition Change) lidar working group has strongly advocated to develop
39 powerful ground-based water-vapour lidar systems with UTLS capability, with focus on the Raman lidar
40 technique. Several Raman lidar systems have already reached a reasonable UTLS performance (Congeduti et al.,
41 1999; Whiteman et al., 2010; Dionisi et al., 2012; Leblanc et al., 2012; Dionisi et al., 2015; Vérémes et al.,

1 2019). Whiteman et al. (2010), Leblanc et al. (2012) and Vèrèmes et al. (2019) demonstrated vertical ranges
2 extending to more than 20 km a.s.l. for averaging over many hours.

3 The most important detection barrier in the lower stratosphere is the very small mixing ratio of water vapour of 4
4 to 5 ppm (e.g., Hurst et al., 2011). In principle, this would require a highly sensitive approach. Measurements of
5 molecules in a range far below one part per trillion with respect to normal conditions can be achieved in the
6 laboratory even under restrictive conditions (e.g., Trickl and Wanner, 1983; Trickl et al., 2010b). However, a
7 fluorescence lidar approach cannot be used for atmospheric H₂O because it electronically absorbs in the vacuum
8 ultraviolet spectral region and undergoes photo-dissociation as concluded from the diffuse bands (e.g., Yoshino
9 et al., 1997). As a consequence, lidar measurements of H₂O in the lower atmosphere are restricted to the
10 differential absorption lidar (DIAL) and Raman scattering methods. The detection sensitivity and the range of
11 the DIAL method is limited by the signal noise of the absorption measurement. Raman scattering is the least
12 sensitive approach. However, night-time Raman scattering is a so-called background-free method. Thus, the
13 sensitivity for water-vapour can, in principle, be driven to any level by enhancement of the laser power and the
14 diameter of the receiver, as long as allowed by financial or technical restrictions. Very importantly, a Raman
15 lidar can be operated at wavelengths for which absorption in the atmosphere is negligible.

16 For a Raman lidar calibration with an external source is an important issue: The optical transmission data of a
17 Raman lidar and the Raman scattering cross sections cannot be determined with sufficient accuracy. In addition,
18 a degradation of the components must be taken into consideration. Thus, a trace-gas Raman lidar routinely
19 operated over an extended period of time must be repeatedly calibrated with external references and the stability
20 of the calibration must be verified. Mostly, radiosonde measurements are used as reference (e.g., Leblanc and
21 McDermid, 2008; Dionisi et al., 2010), but also calibration with H₂O column measurements are reported (Barnes
22 et al., 2008; Vèrèmes et al., 2019). However, the Raman lidar systems are not necessarily located at routine
23 balloon sounding stations. Even for on-site sonde launches the sondes usually rapidly drift away from the lidar
24 which frequently results in discrepancies due to the high spatial variability of water vapour (Vogelmann et al.,
25 2011; 2015). Infrequent comparisons with sondes necessitate additional performance control such as built-in
26 lamps (Dionisi et al., Leblanc and McDermid, 2008; 2011; 2012; Whiteman et al., 2011) or monitoring the
27 radiation backscattered from air or nitrogen.

28 At Garmisch-Partenkirchen, we first concentrated on the differential-absorption-lidar (DIAL) technique for
29 measuring free-tropospheric water vapour (Vogelmann and Trickl, 2008; Trickl et al., 2013-2016; 2020a). This
30 system has the great advantage of a good daytime performance. In recent years a high-power Raman lidar has
31 been built that extends the range of the DIAL into the lower stratosphere during night-time with a data-
32 acquisition time of just 1 h. Both systems are operated side by side at the Schneefernerhaus mountain station
33 (UFS, Umweltforschungsstation Schneefernerhaus, 47° 25' 00'' N, 10° 58' 46'' E) at an altitude of 2675 m,
34 which offers the possibility of direct and accurate calibration of the Raman lidar. The DIAL has been thoroughly
35 validated and is free of bias at an uncertainty level of 1 % of average concentrations or less (Vogelmann, et al.,
36 2011; Trickl et al., 2016). Both system probe the same atmospheric volume and can be very reliably compared
37 up to about 8 km where the DIAL data start to become noisy.

38 The large system allows us to make temperature measurements up to the mesosphere based on an established
39 approach for inverting the Rayleigh backscatter signal for 355 nm (Hauchecorne and Chanin, 1980). In this way,
40 not only the primary green-house gas, but also the most important climate parameter is provided.

41 In this paper we report the development and the current state of the Raman lidar, before the beginning of routine
42 measurements. We describe the steps to achieve up to 180 W of linearly polarized and single-line output from a

1 modified industrial xenon-chloride laser (308 nm) (Sect. 2), and the development of the far-field receiver
2 receiver featuring a primary mirror with a diameter of 1.5 m (Sect. 3). Parallel to the ozone DIAL at IMK-IFU
3 (Trickl et al., 2020b) a significant step forward in signal processing was made. The highly satisfactory lidar
4 performance is demonstrated by examples of 1-h atmospheric measurements, also including a first demonstration
5 of a temperature measurement up to 87 km (Sects. 4 and 6). Finally, conclusions and suggestions for upgrading
6 the lidar are made (Sect. 7).

7 **2 Laser System**

8 **2.1 General Description**

9 Figure 1 gives an overview of the transmitter section of the new UFS Raman lidar system in the rear part of the
10 lidar laboratory (see also Table 1). The transmitter consists of a high-power laser, a hydrogen Raman shifter and
11 a motorized (Astro System Austria, ASA) beam steering mirror (not shown). The 0.5-m-diameter beam-steering
12 mirror sending the radiation into the atmosphere is located in a vertical emergency exit shaft outside the
13 laboratory. All dielectrically coated optics, in particular the large-diameter mirrors, were supplied by Laseroptik
14 G.m.b.H. unless explicitly stated differently.

15 The efficiency of Raman scattering scales as λ^{-4} and, thus, is the highest in the ultraviolet (UV) spectral region.
16 Here, the by far most powerful radiation sources are excimer lasers. The radiation source used in our system is a
17 big XeCl laser system with a power of 350 W (pulse energy 1 J, repetition rate 350 Hz, pulse length 80 ns) in
18 energy-stabilized mode of operation that is normally used for industrial applications (Coherent Göttingen
19 (formerly: Lambda Physik), model Lambda SX 350C, size (l×w×h) = 2.500 m × 0.850 m × 1.925 m). The very
20 high power of this laser system is much more important than the single-pass absorption loss in stratospheric
21 ozone at the operating wavelength of 308 nm (Sect. 4.4). An ozone correction can be provided by a DIAL
22 approach with an “off” emission at 353 nm (stimulated Raman shifting the laser radiation in H₂) or at 355 nm
23 (frequency-tripled Nd:YAG laser).

24 The laser was transported to UFS by a cogwheel train of Zugspitzbahn A.G. There, it could be lifted to the 7th
25 floor of the building with the large elevator of UFS and then to the 8th floor with two pulleys, after removing the
26 stairs.

27 As a consequence of its primarily industrial application, the laser system is operated under computer control
28 providing energy stabilization and numerous safety features. This is highly helpful for the planned automatic
29 operation of the lidar system. However, a high beam divergence of nominally 1 mrad and 4 mrad in two
30 perpendicular transverse orientations, random polarization and a three-line spectrum as shown in Fig. 2 are
31 insufficient for the requirements of the lidar. Therefore, an approach had to be found for overcoming these
32 disadvantages, considering the dangerous power level of this laser.

33 For our lidar concept a linearly polarized narrowband radiation is needed. Injection seeding with a XeCl master
34 oscillator with these properties was the premier choice because this could have resulted in maintaining high
35 average power. However, this idea was given up because of the manufacturer pointed out that there was no easy
36 way of synchronization because of the specified 25- μ s pulse-to-pulse jitter of the big laser, and because of the
37 considerable additional complexity and costs.

38 Instead, an intra-cavity solution was chosen. The resonator was stretched as shown in Fig. 3. The intra-cavity
39 laser beam is first converted to an approximate squared cross section with another 2.5:1 cylindrical telescope in
40 order to reduce the intensity in the new rear section. It is then fed through a Brewster-angle thin-film polarizer
41 (transmittance 96 %) and a custom-made 70-mm-diameter Fabry-Perot etalon with 0.10 mm plate distance (SLS

1 Optics Ltd.; $R = 54\%$, $T_{\min} \approx 7\%$, $T_{\max} = 95.4\%$) to reach the 75-mm-diameter end mirror. The large diameter
2 of the etalon is expected to provide strong reduction of ablation of material by scattered UV radiation and the
3 resulting ageing of the etalon plates. The chosen plate distance sets the free spectral range exactly to twice the
4 wavelength difference between the two groups of emission lines in Fig. 2. When setting the transmission
5 maximum to the short-wavelength component (307.955 nm; all wavelengths in this paper are specified for
6 vacuum) the gain at the wavelength pair around 308.2 nm is suppressed, despite the residual transmittance of
7 about 7%. Just the direct first-pass forward emission estimated by the manufacturer to about 7 mJ cannot be
8 avoided.

9 The beam divergence with our long cavity was smaller than that determined by the manufacturer. We measured
10 a burning spot of $2.0 \times 1.2 \text{ mm}^2$ generated on a metal plate by focussing with a $f = 2.0\text{-m}$ lens in front of the
11 Raman shifter, corresponding to a divergence of $1.0 \times 0.6 \text{ mrad}^2$. After the 5:1 beam expansion the beam
12 divergence is 0.2 mrad or less, an important prerequisite for ensuring a moderate size of the focal areas in the
13 very large receiver and its polychromator. As explained further below the final focal length is 1.75 m, resulting
14 in a slightly better-collimated beam.

15 **2.2 Laser Testing**

16 ***General Remarks***

17 Despite the pronounced intra-cavity losses after multiple passes through the laser cavity the maximum pulse
18 energy achieved at repetition rates below 100 Hz is about 0.75 J. We explain this by fresh gain generated all
19 along the 80 ns of laser emission and by 92% of the amplified energy being emitted after each round trip. Thus,
20 the losses do not matter similarly as in a cavity with higher reflectance of the output mirror.

21 ***Emission Spectrum***

22 For the laser operation we just slightly tilted the etalon vertically in order to avoid specular reflection. The
23 wavelength is changed by horizontally tuning the etalon that is mounted on a motorized rotation stage (OWIS).

24 For monitoring the emission spectrum an inexpensive computer-controlled miniature grating spectrograph is
25 used (Ocean Optics, HR 4000; $\Delta\lambda = 0.07 \text{ nm}$). The performance of this spectrograph is highly satisfactory and
26 stable as determined from a comparison of the 308.955-nm emission that is reproducibly obtained for maximum
27 laser emission. Both the emissions around 308 nm and 353 nm are within the limited measurement range.

28 In Fig. 4 we show a typical spectrum obtained with the HR 4000 spectrograph. The etalon was rotated to
29 concentrate the pulse energy is concentrated almost exclusively in the low-wavelength spectral component. The
30 etalon angle was not fully optimized to show the small impurity peak at 308.4 nm that is located at twice the
31 distance between the strong line groups in Fig. 2 and is, thus, most likely corresponds to another, weaker line of
32 XeCl. Under optimum conditions the impurity stays in the range between 1.0 and 1.5%. Further suppression
33 would require an etalon with a slightly larger free spectral range.

34 The contribution of the longer-wavelength doublet (308.2 nm) for an optimum etalon angle is less than 0.5%.
35 This value is in reasonable agreement with the 7 mJ of initial forward emission (Sect. 2.1), considering that just
36 one half of this weak broadband emission goes into the correct wavelength component (Fig. 2).

37 Given the specified 0.07-nm resolution of the HR 4000 spectrograph the laser bandwidth is approximately 0.03
38 nm. in good agreement with the 0.0357 nm in the spectrum measured by Coherent in a high grating order (Fig.
39 2).

1 It is interesting to note that with an initially pronounced vertical tilt of the etalon we had achieved continuous
2 single-line tuning of the laser, however with changing output pulse energy as a function of the horizontal tilt
3 angle.

4 ***Polarizer***

5 Linear polarization is mandatory for single-line stimulated Raman shifting (Kempfer et al., 1994) and for the
6 wavelength-separation strategy in our receivers (Sec. 3.2). Therefore, a thin-film polarizer was mounted in the
7 extended laser cavity, in the expanded section of the beam where the intensity is reduced. Despite the widened,
8 quadratic beam profile the substrate and the holder get rather warm after long operation of the laser at full power.
9 This is caused by the absorption losses due to a maximum transmittance of just 94 %. Nevertheless, the degree
10 of polarization of the laser output is as high as 99.4 %, in agreement with the expected 3.5 mJ (Sect. 2.1) of
11 forward emitted radiation with wrong polarization after the first passage through the laser medium.

12 Laseroptik meanwhile promised the capability of producing thin-film polarizers with more than 99 %
13 transmittance (as demonstrated for the polychromator). This would significantly reduce the thermal load and the
14 intracavity radiation losses.

15 ***Alignment drifts***

16 A careful warm-up procedure was seen as mandatory because of the long resonator. Any small thermally
17 induced misalignment leads to a pronounced rotation of the laser beam inside and outside the cavity which can
18 lead to damage of components. Horizontal misalignment of the cavity starts to progress with growing repetition
19 rate that requires to rotate both the etalon and the end mirror horizontally. If the optical surfaces of the etalon
20 stay perfectly parallel the latter is difficult to understand and is tentatively ascribed to a combination of a slight
21 mutual distortion of the etalon plates and the cylindrical telescope. Vertical corrections are mostly negligible.

22 Warm-up has been performed in 50-Hz steps. For each step, etalon and end mirror are realigned for maximum
23 power after about five minutes of thermal equilibration. Very importantly, maximum power corresponds to
24 optimum beam pointing and optimum spectral purity, which is highly welcome in view of automatic control of
25 the modified laser. At the end a highly stable operation of the laser is achieved over many hours rarely requiring
26 intervention.

27 For safety, six sand-blasted aluminium apertures were added as shown in Figs. 1 and 3, the first five of them
28 with a cross section of $43 \times 43 \text{ mm}^2$, the last one in the expanded beam, (width = 200)×(height = 120)- mm^2 . As
29 mentioned, inside the laser cavity even weak reflections can lead to damage at maximum repetition rate. Outside
30 the laser head the apertures also help to control the beam pointing. At full power metal plates must be used to
31 localize the beam instead of paper sheets.

32 ***Laser Pulse Energy***

33 In Fig. 5 the dependences of the pulse energy on repetition rate and load voltage, measured with the modified
34 system, is shown. For each measurement both end mirror and etalon were optimized.

35 The maximum pulse energy for a load voltage of 1.95 kV was 797 mJ without etalon and 765 mJ with the etalon
36 installed. This is much less than the 1.24 J at 1.95 kV and 300 Hz repetition rate achieved with the laser at the
37 factory. Of course, there are considerable intra-cavity losses. These losses are mostly caused by the polarizer and
38 the etalon, but perhaps also by deficiencies in imaging in the cylindrical telescope or by achieving less round
39 trips within the elevated-gain period due to the longer cavity. However, the overall losses are considerably

1 stronger than the optical losses, as we estimate from the moderate reduction in pulse energy when inserting the
2 etalon. We conclude that the most important drop in power is caused by the reduced number of round trips in the
3 extended cavity.

4 With growing repetition rate the energy first increases, but above 150 Hz it starts to drop considerably. This
5 behaviour is not similarly pronounced without the etalon as shown for comparison. It is, thus, ascribed to thermal
6 stress in the etalon. The optimum pulse energy at 350 Hz achieved for clean optics was 515 mJ, resulting in a
7 power of 180 W, one order of magnitude higher than in 355-nm Nd:YAG-based water-vapour Raman lidar
8 systems in the past. The power slowly decreases further during a long night-time measurement period, most
9 likely due to growing thermal issues. Under typical conditions we have operated the lidar in the range of 400 to
10 450 mJ, with aged gas even less. The pulse repetition rate was set to 300 Hz because of a time limitation in the
11 data-acquisition system for operation with 16000 bins.

12 The pulse energy at low repetition rate rises from 499 mJ at 1.55 kV to 777 mJ at 2.0 kV (lower panel of Fig 5).

13 **2.3 Raman Shifter and Beam Expander**

14 As routinely done in stratospheric ozone DIAL systems we first applied stimulated Raman shifting in high-
15 pressure hydrogen for generating an “off” wavelength of 353.144 nm (Sec. 3.2) as a base for ozone corrections
16 and a high-altitude temperature Rayleigh detection channel. We assumed that a conversion efficiency of a few
17 per cent are sufficient for these purposes. In this way we could fulfil two goals, to minimize the loss of pulse
18 energy in the fundamental wavelength for maximizing the detection sensitivity for water vapour, and to reduce
19 the uncertainty in the pulse-energy level at 308 nm needed for calibration of the H₂O Raman detection channel.

20 One traditional problem with stimulated Raman shifting are losses due to the generation of high Stokes orders
21 and due to optical breakdown, that can, according to our experience, efficiently be accomplished even with a
22 long focal length of 1 m (Kempfer et al., 1994; Trickl et al., 2020b). Thus, we followed the design of the
23 stratospheric ozone DIAL at Table Mountain (McDermid et al., 1991, and personal communication) and first
24 selected an $f = 2.0$ m focussing lens. The length of the high-pressure cell is 3.6 m.

25 Indeed, the measurements at low repetition rates confirmed that just the first Stokes order was generated and the
26 transmitted pump and Stokes energies summed up to 100 %. For 780 mJ emitted by the laser (without etalon) at
27 a repetition rate of 10 s^{-1} 19 % conversion into the first Stokes order was measured. However, the 353-nm
28 energy conversion efficiency at high repetition rates did not exceed 3 % at a repetition rate of 350 Hz.. This
29 required very critical astigmatic focussing influenced by a cylindrical beam expander in front of the laser (no
30 longer used, therefore missing in Fig. 1). With a well-collimated laser beam no conversion was achieved at all at
31 repetition rates beyond 100 Hz, even when we lowered the threshold energy with the finally used $f = 1.75$ -m lens
32 (Fig. 1).

33 A new approach was introduced that is described below. The Raman shifter was then used just as a vacuum cell
34 for the beam expander to avoid optical breakdown in air.

35 **2.4 New Approach with a Frequency-Tripled Nd:YAG Laser**

36 Instead of spending more time for Raman-shifting experiments, e.g., with longer focal lengths or a pair of
37 crossed cylindrical lenses (Perrone and Picinno, 1997), we integrated in 2018 the injection-seeded Nd:YAG laser
38 previously used in the water-vapour DIAL (Continuum, Powerlite 8020 Precision) into the system. This laser,

1 modified for optimum beam quality for pumping a single-mode optical parametric oscillator, yields a reduced
2 third-harmonic (355 nm) pulse energy of 160 mJ at a repetition rate of 20 Hz. This is sufficient for reasonable
3 measurements (Sect. 6.2).

4 The use of this laser for providing the “off” wavelength has two advantages. Firstly, the full, stable power of the
5 XeCl laser is available for the sounding of water-vapour, important for the H₂O calibration. Secondly, the
6 Nd:YAG laser is run delayed with respect to the XeCl laser. In this way interference of the 355-nm Rayleigh
7 return in the H₂O Raman channel is completely excluded.

8 The Powerlite laser is meanwhile operated under control of an external computer, and synchronized with the
9 XeCl laser.

10 **2.5 Conclusions for the laser system**

11 Based on previously available laser specifications we had planned an average laser power of about 200 W,
12 ensuring an order-of-magnitude increase with respect to frequency-tripled Nd:YAG lasers most commonly used
13 in this field. Thus, the maximum single-line output of 180 W achieved in this project is acceptable. Also the high
14 degree of polarization fulfils the requirements for the new lidar.

15 Nevertheless, the significant loss of power with respect to the free-running laser is a major disappointment.
16 Solutions could come from injection seeding or shortening the laser cavity. We currently exclude injection
17 seeding since this would add significant costs and complexity. Shortening means a removal of the cylindrical
18 beam expander. This would enhance the intensity in both the etalon and the thin-film polarizer. However, as we
19 learnt from Laseroptik, both optics can be meanwhile manufactured almost without optical loss. In this way, the
20 thermal problems are minimized.

21 An important result is that for maximized output the beam pointing is extremely reproducible. Because of this
22 property we have meanwhile started to develop automatic power optimization by horizontal rotation of both the
23 etalon and the end mirror.

24 **3 Receiver design**

25 **3.1 General Design Considerations**

26 As also pointed out by Trickl et al. (2020b) the receiver design of the IFU lidar systems follows a number of
27 design principles:

- 28 (1) We use Newtonian telescopes for a less critical alignment.
- 29 (2) We separate the return in near-field and far-field channels because of the giant dynamical range of the
30 backscatter signal (see Sec. 4.3).
- 31 (3) No optical elements or detectors are placed close to the focal points in order to avoid a modulation of the
32 backscatter signal by the near-field scan of the focal point across inhomogeneously transmitting or detecting
33 surfaces. This prohibits the use of optical fibres because of their unknown input surface quality (apart from
34 coupling losses which mean throwing away a lot of the costly laser photons).
- 35 (4) Particularly inhomogeneous surfaces (such as those of the photomultiplier tubes (PMTs) used in our
36 system) are placed in or very close to image planes (exit pupils) where the image spots and the light bundle
37 as a whole stay stable in space. This also ensures that drifts in laser pointing have no influence on the
38 position of the spot of the returning radiation on the detectors even for very long beam paths, resulting in a
39 long-term stability as long as the no part of the light bundle is cut off by a holder or an aperture.

- 1 (5) The expensive interference filters are also placed in exit pupils to keep their diameter as small as possible.
2 The interference filters are placed in a collimated part of the radiation bundle to minimize angular spread. In
3 this way the near-field overlap is maximized.
- 4 (6) All lenses with focal lengths below 0.2 m are anti-reflection coated in order to avoid angle-dependent
5 transmittances.

6 3.2 Telescopes

7 Two separate Newtonian telescopes are used with focal length $f = 2$ m and diameter $d = 0.38$ m (Intercon
8 Spacetec, taken from our former eye-safe aerosol lidar (Carnuth and Trickl, 1994; Trickl, 2010), and with $f = 5.0$
9 m, $d = 1.50$ m (Astrooptik Philipp Keller), respectively. The large focal length of the far-field telescope
10 necessitated to install the receiver system in a separate tower on the terrace above the lidar (Fig. 6). The tower
11 (Sirch and Hägele&Böhm) is covered by a 4.2-m-diameter astronomical dome with a 1.50-m slit (Baader
12 Planetarium) which had proved to be an adequate solution under the arctic conditions on the high mountain. The
13 entire structure is designed for withstanding wind speeds up to more than 300 km h^{-1} . The costs for the dome
14 limit its size, and the slit width determines the width of the large telescope. Tower and dome were transported to
15 the site by a big Kamov double-rotor helicopter (HELISWISS), the large mirror with a small helicopter from
16 Heli Tirol. The mirror was lowered to the terrace, from where it was moved into the tower under assistance of
17 two provisional cranes.

18 Although the frame of the large telescope is prepared for heating this turned out to be unnecessary because of a
19 powerful heating system inside the tower. The tall frame carries both the secondary mirrors and the two
20 polychromators without contact to the measurement compartment that is stepped on by the operators. The tower
21 can be entered by two doors at the terrace level and upstairs. The upper door allows us to access the
22 measurement compartment directly or to use the emergency exit also after a major snowfall.

23 3.3 Polychromators and Wavelength Separation

24 The final design of the polychromators is shown in Fig. 7. The optical table (OPTA G.m.b.H.) is in reality
25 oriented vertically with the left-hand side representing the top. The entrance of the radiation arriving from the
26 telescope is horizontal (see Fig. 8), i.e., rotated with respect to the drawing plane, as one can see from the change
27 in polarization vector (dot for out-of-plane to double arrow for in-plane orientation). The radiation bundle is
28 spatially filtered with a rectangular aperture with four adjustable blades (custom-made by OWIS) placed in the
29 focal plane. Due to space limitations the aperture is oriented perpendicularly to the beam axis. A slight tilt angle
30 would be superior because of the longitudinal walk of the “focus”. This will be made possible in the future by
31 mounting additional inclined apertures in front of the PMTs. In this way, also the different diameters of the focal
32 points, caused by the different beam divergences of the two lasers, can be accounted for.

33 Several relay-imaging modules formed by confocally arranged $f = 150$ mm lenses (f_1) are seen (Sec. 3.1; see also
34 (Vogelmann and Trickl, 2008)). In the sections with parallel beams (with one exception) beam splitters and
35 interference filters are placed in or close to image planes of the primary mirror. Another confocal pair of f_1
36 lenses (not shown) is used to transfer the radiation from the focus of the large telescope to the first focal point in
37 the polychromator. The short-f lenses (f_2) image the principal mirror on to the photocathode of the
38 photomultiplier tubes (PMTs). The exact positions of the intermediate and final exit pupils can be nicely
39 identified with visible sky light after removing the interference filters.

1 The specifications of the polychromators are listed in Table 2, including the lidar vacuum wavelengths and the
2 Raman shifts used. The Raman shifts in Table 2 sometimes differ from those in the lidar literature. The radiation
3 for the different wavelengths are separated by dichroic beam splitters and narrowband interference filters. This is
4 a highly demanding task considering the eight to ten orders of magnitude in signal between the Rayleigh and
5 Raman channels (Sec. 4.3). Figure 7 shows the principal polychromator design without the black walls
6 separating the detection compartments or surrounding the filters. In order to save costs, the optics of both
7 polychromators are equal for except for focal length f_2 that is chosen to achieve image diameters of the order of
8 5 mm for the different primary mirrors.

9 The optics (Table 3) were mostly purchased from Laseroptik G.m.b.H., with the exception of the narrow-band
10 interference filters and the steep-edge long-pass beam-splitters 5 and 6 (Materion Barr; beam splitter 6 is not
11 shown in Fig. 7). The width of the interference filter for water vapour (347 nm) was chosen to cover the entire
12 rather wide Q branch of H₂O in order to avoid a temperature influence on the backscatter profiles. A broad-band
13 interference filter (IFB; Semrock; T = 85-90 %) was recently added for additional suppression of a potential
14 residual influence of radiation outside the wavelength range of the Raman returns such as scattered light from
15 illuminations inside the laboratory, from the buildings of the ski area or residual 308-nm contributions.

16 The design in Fig. 7 differs for the two long-wavelength channels from that described by Klanner et al. (2012),
17 used until 2017. The old approach to separate the 347-nm and 353-nm returns was based on a pair of beam
18 splitters with steep spectral edge (BS 6 in Table 3) similar to those used for separating the N₂ channel. The
19 angular alignment for optimum H₂O signal was very critical, which is not helpful for a stable performance with
20 stable calibration. The modifications in Fig. 7 remove the alignment-dependent signal loss in the H₂O channel.
21 They benefit from the new laser concept (Sect. 2.3): The 355-nm pulses are temporally shifted with respect to
22 those at 308 nm. In this way any residual 355-nm interference in the 347-nm channel is avoided.

23 Some of the components have been replaced by new ones with better performance over the years, i.e., polarizing
24 beam splitter 1 (R > 99 % for 308 nm), and the interference filter in channel 2. The latter filter now suppresses
25 radiation at the pump wavelength to a level of about 2×10^{-4} . The low transmittance of the shorter-wavelength
26 interference filters is disappointing, but slightly exceeds that quoted. However, T = 55 to 65 % for a $\Delta\lambda = 0.1$ -nm
27 filter has been achieved at 386.7 nm by the same manufacturer in the past (Whiteman et al., 2010).

28 **3.4 Detectors and Discriminators**

29 The detector choice is based on the experience from our stationary ozone lidar system. The final development
30 stage took place parallel to that for the ozone DIAL and is described in detail in (Trickl et al., 2020b).
31 Hamamatsu R7400U-03 tubes were chosen and integrated in an actively stabilized socket optimized for us in
32 1999 for our three-wavelength aerosol lidar by Romanski Sensors (RSV). The socket is now modified to deliver
33 optimized single-photon spikes without the ringing of the original PMTs that had previously enhanced the count
34 rate in our ozone DIAL up to about 5 km (Fig. 8). Signal-induced nonlinearities can be avoided for normal
35 operating voltages around 800 V if one limits the analogue signal to roughly 100 mV or less (Trickl et al.,
36 2020b). This level is high in comparison with traditional PMTs. Nonlinearity in the photon-counting signal
37 revealed by a comparison with a simultaneous ozone measurement at Hohenpeißenberg for analogue signals of
38 400 mV

39 The output of a PMT is fed into an impedance-matched junction containing the discriminator (RSV). The output
40 for the analogue channel is slow, with single-photon pulses widened by a factor of two. The second branch is the
41 fast discriminator that emits -0.4-V constant amplitude pulses with a full width at half maximum of 0.6 to 1.5 ns,

1 depending on the photon pulse height. The discriminator level that can be chosen from -2 mV to lower voltages.
2 This is important for the six-dynode PMT and its rather small pulses. The pulse-height distribution for 800 V
3 peaks at about 10 mV (Fig. 9). We have applied discriminator levels between -4 and -5 mV.

4 An important issue for achieving a high sensitivity is a low level of dark counts photons, which normally
5 requires to cool the PMT (0.03 counts s^{-1} : Trickl and Wanner, 1981). With the PMTs used here and
6 discriminator levels of -4 mV no dark count was registered in 50-ns bins within one hour (1×10^6 laser shots)
7 without cooling. The average external background for atmospheric measurements is clearly less than 1 count for
8 voltages up to the maximum of 1000 V, except for the H_2O channel (see Sect. 6).

9 **3.5 Transient Digitizers**

10 Following the other lidar systems developed at IFU since 1995 we purchased two 12-bit, 20 Hz transient
11 digitizer systems from Licel, each with six channels. Licel designed for this project and the ozone DIAL new,
12 ground-free input amplifiers. This latest version has led an unprecedented performance in the ozone DIAL with a
13 relative noise level of about $\pm 1 \times 10^{-6}$ of the full voltage range after minor smoothing, yielding also highly
14 sensitive aerosol measurements at 313 nm despite the short wavelength (Trickl et al., 2020b).

15 An exponentially decaying contribution of roughly 10^{-5} of the peak signal is present that scales as the signal
16 pulse area, i.e., grows with the wavelength. After introducing the discriminator for the photon-counting channel
17 and the counter the exponential wing increased and a slight undershoot occurred in addition. The interference
18 could be strongly reduced by adding an optocoupler to the trigger input of the counting system (Sect. 3.6). Some
19 more sophisticated impedance matching is necessary for achieving an ultimate performance. Examples for the
20 performance so far achieved are shown in Sect. 6.

21 Another limitation has resulted from the high data transfer produced by the chosen 16000 bins (120 km): The
22 repetition rate of the laser had to be limited to 300 Hz in order to allow for a reliable data storage.

23 **3.6 Photon counting**

24 Single-photon counting is mandatory in a lidar system with stratospheric capability. In order to benefit from the
25 temporal resolution of the PMTs we purchased MCS6 and one MCS6A five-channel photon counting systems
26 from Fast Comtec. Just two of them were used at the end since the analogue signal range for the near-field
27 receiver was found to be good enough to do without photon counting. The signals are scanned for falling edges
28 at intervals of 100 ps which means a maximum count rate of about 5 GHz for equidistant picosecond pulses.

29 A bottle neck of this counting system is the sequential data transfer to the computer that limits the signal to
30 $1.8 \times 10^7 s^{-1}$. The multi-channel scaler was, therefore, triggered with a delay of 10 to 20 μs with respect to the
31 laser pulse which resulted in a fully linear performance for H_2O . However, if an earlier beginning of the
32 individual measurement is desired on-board averaging becomes necessary that is not implemented in this model.

33 Another limiting issue has been the control program of the counting system: An automatic start from outside
34 UFS is not reliable and, thus, a “mouse click” on the “start” symbol is needed on the remote computer.

35 **3.7 System Control**

36 The electronic components of the two DIAL systems (Ingenieurbüro W. Funk) are ground-free. The trigger pulse
37 is derived from a photodiode and subsequently distributed into numerous output channels via optocouplers. The
38 supply voltages are transferred to the different devices in shielded cables. The shields of the cable leading to the

1 PMTs are open on the side of the detectors. The supply voltage can be set by the lidar PC via an I²C bus. Electro-
2 magnetic interference in the lidar signals from outside (e.g., the laser) has been kept at a negligible level by using
3 doubly shielded cables (Suhner, G03332; the outer shield is left open on one side) and ground-free circuits.
4 The data acquisition of the lidar system is controlled from a central Linux computer via a perl program and
5 ethernet. The Licel transient digitizers are fully read every 10 seconds. At a repetition rate of 300 Hz this allows
6 for an integration without overflow due to 24-bit depth for each unit. This data stream is subsequently integrated
7 for each channel by the controlling program until the end of the measurement after one million laser shots
8 corresponding to an integration time of roughly one hour. The measurement data is finally stored in an ASCII
9 file including meta information in the file header.
10 The same perl program is designed to control also the photon counting devices via ethernet communication with
11 the Windows based FASTComTec software. As mentioned, this communication does not yet work reliably for
12 control from outside UFS.
13 Meanwhile, the excimer laser can be operated via Ethernet, as well as the rotation of the etalon, the spectrometer
14 HR400 and a new motorized end mirror of the XeCl laser. The laser power supply and cooling water pump are
15 controlled by Wago-SPS units (programmed in CodeSys) via a Java web interface. The beam steering mirror is
16 motorized and remotely controlled with a custom made software from ASA. The slit of the lidar dome, the
17 covers of the telescopes, the laser output mirror and the power supply of the lidar receiver are controlled with a
18 Wago-SPS system via a Java Web interface.

19 **4 Data Processing**

20 **4.1 Water Vapour**

21 A great advantage of a Raman lidar is that uncalibrated H₂O densities are obtained in a robust way by
22 multiplying the backscatter signal for the full ro-vibrational Q branch by the square of distance r (range
23 correction). Thus, small perturbations of the signal do not matter as severely as in the DIAL algorithm that
24 implies derivative calculations. However, in our system the choice of a particularly powerful UV laser
25 implicated a short operating wavelength of 308 nm. Thus, for obtaining number densities an ozone correction
26 must be made that is based on the DIAL solution for the wavelengths 307.955 nm and 353.11 nm (or recently
27 354.22 nm).

28 For simplicity we have so far preferred to calculate just water-vapour volume mixing ratios, which also makes a
29 range correction superfluous. The uncalibrated mixing ratios are calculated by dividing the H₂O backscatter
30 signal by the vibrational nitrogen Raman backscatter signal. Here, the influence of ozone exactly cancels on the
31 upward path because the transmitted wavelength is the same for both Raman channels. On the downward path a
32 small residual absorption in the stratospheric ozone exists at 331.75 nm that grows to almost 2 % at 20 km and
33 has been neglected given the current level of accuracy at this altitude. The photon counting data are collected at
34 51.2 ns per bin instead of the 50 ns in the transient digitizers and are interpolated to match the time scale of the
35 analogue data. In order to avoid excessive data array sizes, we double the bin size to 100 ns during the
36 subsequent calculations, averaging pairs of neighbouring signals,

37 In the useful range for H₂O up to roughly 20 km the relative noise of the nitrogen Raman signal is negligible and
38 no smoothing is applied. Smoothing is just applied to the Raman signal ratios that are determined separately for
39 the analogue and the photon-counting data. The smoothing approach is based on a numerical low-pass filtering
40 approach with Blackman window described and characterized in the parallel paper by Trickl et al. (2020b). This

1 numerical filtering approach is free of ringing. The filtering interval is dynamically increased. As shown in Sec.
2 6 a purely quadratic dependence

$$3 \quad L = 1.2 \times 10^{-4} i^2$$

4 as a function of 15-m bin i (minimum interval size: 2 bins, $i \leq 300$) (or slightly modified for noisier data) is
5 adequate. In one case (5 February 2019) a third-order polynomial was used for L to achieve a better vertical
6 resolution in the lowermost stratosphere in the presence of a steep concentration feature. In a Raman lidar this
7 dependence does not require much modification from measurement to measurement, whereas in a DIAL the
8 strongly changing water-vapour concentration results in considerable change in absorption and, thus, of the
9 smoothing requirements. The definition of vertical resolution so far used by us is given by the range interval
10 corresponding to the 25 % to 75 % rise of the response of the smoothing filter to a Heaviside step (VDI, 1999).
11 For the Blackman filter the VDI vertical resolution is 19.3 % of the size of the smoothing interval. Leblanc et al.
12 (2016) recommend to define the vertical resolution as the full width at half maximum of a delta response which
13 is 34.7 % of the filtering interval for the Blackman filter. Equation 1 yields a VDI vertical resolution of 155 m at
14 10 km, 348 m at 15 km and 619 m at 20 km, and a delta-response vertical resolution of 277 m at 10 km, 624 m at
15 15 km and 1109 m at 20 km.

16 The role of aerosols is limited to extinction and, in the case of biogenic particles (Immler et al., 2005; Reichardt
17 et al., 2017), to fluorescence in a Raman lidar. The presence of aerosols is best judged from the 355-nm channel.
18 The influence of extinction is very low when calculating the H₂O mixing ratio from the ratio of the H₂O and N₂
19 profiles. An estimate of the extinction coefficients at the two wavelengths can be obtained from the 355-nm data.
20 The system testing was limited to clear nights. Thus, aerosol effects could be neglected.

21 **4.2 Temperature**

22 The retrieval of temperature from lidar data is a highly demanding task. For instance, an uncertainty of 1 K
23 means a relative uncertainty of 0.33 % at a temperature of 300 K. Thus, a very high quality of the backscatter
24 signals is a prerequisite for reasonable results. For our system the two conventional methods have been selected,
25 evaluating the temperature dependences of the rotational Raman spectra received just below 308 nm (Arshinov
26 et al., 1983) and the direct retrieval of temperature from backscatter profiles (Hauchecorne and Chanin, 1980).

27 The retrieval of temperature profiles from rotational Raman backscattering has not yet been optimized and is,
28 thus, not described here. The main problem has been that the first generation of 307.390 nm interference filters
29 obtained from Materion Barr did not sufficiently reject the 307.955-nm contribution. In principle, this
30 contribution is a reasonable reference in the absence of aerosol because it is independent of temperature. Thus,
31 several successful temperature retrievals could be achieved for the near-field receiver (Höveler, 2015).

32 The evaluation of temperature profiles directly from backscatter profiles has been tested for the Rayleigh
33 channels at 308 nm, 353 nm, 355 nm as well as the nitrogen Raman channel (332 nm). Due to the signal losses
34 caused by ozone the range of the N₂ channel is limited. We finally decided to invert the backscatter signal for
35 355 nm (Sec. 2.3). The analogue and photon counting backscatter profiles are merged into a single profile,
36 switching at about 28 km. The resulting profile is, again, smoothed with the Blackman filter mentioned above.
37 Similar to water vapour the filtering interval Δ is enhanced as (approximately)

$$38 \quad L = 2 \times 10^{-5} i^2$$

39 as a function of 15-m bin i .

1 We follow the strategy of calculating the temperature described by Shibata et al. (1986). In a first step the
 2 density is calculated and subsequently the temperature. However, instead of the simplified density algorithm we
 3 use a fully quantitative Klett-type approach with downward integration from the far end (Klett, 1981; 1985). The
 4 result is calibrated to the number density n and not to the backscatter coefficient:

$$5 \quad n(r) = \frac{n(r_{ref}) r_{ref}^2 S(r_{ref})}{r^2 S(r) + 2n(r_{ref}) \sigma_R \left[1 + \int_r^{r_{ref}} r'^2 S(r') dr' \right]}, \quad (1)$$

6 $S(r)$ being the ozone-corrected backscatter signal, r_{ref} the reference distance and σ_R the Rayleigh extinction
 7 coefficient. We take as a first approximation a reference value calculated from NCEP (National Centers for
 8 Environmental Prediction, <http://www.ncep.noaa.gov/>) data. The NCEP values are available up to a geopotential
 9 altitude of roughly 54 km. Beyond this, initial guesses from the U.S. Standard Atmosphere (1976) are taken,
 10 after converting the geopotential altitudes into real ones (as in the case of the NCEP data). The results of the
 11 inversion with Eq. 1 are then compared with radiosonde or NCEP values in a low-noise range of the backscatter
 12 profile at moderate altitudes. If the agreement in this reference range is not sufficient, $n(r_{ref})$ is modified, and the
 13 procedure is repeated until agreement is reached. This approach is highly robust, a change in reference value
 14 corresponding to an approximate parallel shift of the curves. For the selection of r_{ref} , it is advisable to select a
 15 position for which the signal $S(r_{ref})$ is closest to the average of adjacent data points. In this way, the subsequent
 16 correction necessitated by the local data noise are the lowest.

17 The temperature is subsequently calculated from the density by applying

$$18 \quad T(z) = T(z_0) \frac{n(z_0)}{n(z)} + \frac{m_{air}}{k n(z)} \int_z^{z_0} n(z') g(z') dz', \quad (2)$$

19 with z being the altitude above sea level, $m_{air} = 28.9644$ u (U.S. Standard Atmosphere (1976); 1 u =
 20 $1.6605390 \times 10^{-27}$ kg) the mass of an “average air molecule”, and g the gravitational acceleration (Mohr et al.,
 21 2014),

$$22 \quad g(z) = g_0 \left(\frac{r_E}{r_E + z} \right)^2,$$

23 with $g_0 = 9.80665$ m s⁻¹ and the earth radius $r_E = 6356766$ m.

24 Equation 2 immediately shows that selecting z_0 at the upper end of the data-evaluation range means a strong
 25 decrease with the growing density on the way downward. As a consequence, the second term in Eq. 2 clearly
 26 dominates the temperature about 15 km downward from z_0 . Here, the the number density retrieved in the first
 27 step determines the temperature. Any density error critically enters the computation of the temperature. Thus, the
 28 range of the temperature retrieval is shorter than that of the density retrieval.

29 4.3 Uncertainties

30 Uncertainties u of both water vapour and temperature have been approximated by the expression

$$31 \quad u = \sqrt{u_0^2 + \left(u_1 \frac{r^2}{r_{ref}^2} \right)^2 + (u_2 S(r))^2}, \quad (3)$$

1 with coefficients u_0 , u_1 , and u_2 that are adjusted by comparison with reference measurements as shown in the
2 examples in Sect. 6. The second term in Eq. 3, quadratic in r , reflects the quadratic rise of the noise of the
3 unsmoothed quantities. The reference distance r_{ref} is chosen at the upper end of the data evaluation range. By the
4 approach with Eq. 3 considerable computation efforts have been avoided.

5 **4.4 Simulation of the system performance**

6 Before finalizing the lidar design a number of simulations of the system performance were made. Figure 10
7 shows the results for 200 W of laser power at 308 nm, a range bin of 200 m, 10 % detection efficiency and a
8 measurement time of 1 h. The atmospheric data were taken from the mid-latitude summer model of the
9 LOWTRAN simulation program (Kneizys et al., 1988).

10 It is obvious that the Raman backscatter signal for stratospheric water vapour is roughly eight orders of
11 magnitude smaller than the Rayleigh backscatter signal for 308 nm. This imposes extreme boundary conditions
12 for the optical system (Sec. 3.3). The effect of the signal loss at 308 nm due to the absorption by ozone is not
13 very severe up to 20 km. In comparison with the most commonly used primary wavelength of 355 nm this loss is
14 roughly compensated by the fourth-order frequency dependence of the Raman backscatter coefficient.

15 As demonstrated by the atmospheric measurements the polychromators fully meet the requirements.

16 **5 Calibration of the water-vapour profiles**

17 The calibration of the Raman lidar by the water-vapour DIAL operated in the same laboratory is a unique chance
18 to overcome the restrictions imposed by the sometimes extreme variability of water vapour (Vogelmann et al.,
19 2011; 2015). This variability is caused by a rapid sequence of atmospheric layers of strongly different origin.
20 The humidity varies from very high (origin in the boundary layer) to extremely low (origin in the stratosphere).
21 Our routine measurements since 2007 have revealed that on 84 % of our ozone measurement days stratospheric
22 influence could be identified in the free troposphere (Trickl et al. 2020a). This leads to a particularly strong
23 modulation of the humidity profile.

24 In Fig. 11 we show the first example of a comparison between the two lidar systems on 25 April 2013. The
25 measurements took place under highly complex conditions in the presence of three dry layers, two of them
26 clearly related to stratospheric air as follows from the almost negligible humidity. 315-h backward trajectories
27 with the HYSPLIT model (<http://ready.arl.noaa.gov/HYSPLIT.php>; Draxler and Hess, 1998; Stein et al., 2015),
28 run here with re-analysis meteorological data, show a 5- to 7-day descent from altitudes above 9 km over
29 western Canada and more than 10 km above the Aleutian Islands for the layers at 4.2 km and 6.7 km,
30 respectively.

31 This was the only case in our entire test phase in which a slight 308-nm background was superimposed on the
32 signal. This background could be reliably removed by subtracting a very simple exponential curve. After
33 calibration of the data from the Raman lidar with those from the DIAL above 5.5 km reasonable agreement was
34 found in a major fraction of the free troposphere. However, due to using the same electronics in that early phase
35 the measurements were not made simultaneously. Thus, a few differences are visible and ascribed to to
36 sometimes extreme spatial and temporal variability of water vapour (Vogelmann et al., 2011)

37 The strong variability becomes even more obvious from comparisons with the Innsbruck (32 km to the south-
38 east; shown) and Munich radiosonde (100 km to the north; not shown) ascents that differ strongly and do not
39 show similarly dry layers despite similar courses of the trajectories calculated for these sites in comparison with
40 those for the lidar station. This example demonstrates that simultaneous calibration of the Raman lidar with the

1 quality-assured DIAL (e.g., Trickl et al., 2016) is mandatory. Unfortunately, comparisons have no longer been
2 possible after 2014 due to a permanent laser damage of the DIAL. The development of a new Ti:sapphire laser
3 system with high repetition rate is under way and emission was already demonstrated.

4 The stability of the calibration can be monitored by using the signals of the 308-nm, 332-nm and 355-nm
5 channels outside ranges affected by aerosol.

6 During the rest of the test period in part described in the following the system was calibrated by comparison with
7 sonde humidity profiles from Munich, Innsbruck and Hohenpeißenberg, selecting sections of the sonde profiles
8 looking most reasonable. Geopotential altitudes are converted into true altitudes. During one night in February
9 2019 very successful comparisons with a CFH sensor (launched in the valley) were made.

10 **6 Measurements in the Atmosphere**

11 After the completion of the lidar systems testing started in autumn 2012. The measurements demonstrated the
12 perfect suppression of interference from the other channels in the water-vapour channel by spectral filtering and
13 shielding. This achievement implies, according to the simulations in Sec. 4.3, a suppression of more than nine
14 decades of 308-nm background.

15 In early 2015, the near-field receiver was completed and performed well. Even rotational Raman retrievals with
16 a temperature noise level of 1 K were achieved (Höveler, 2015). In addition, single-photon counting successfully
17 entered operation for the far-field receiver, but was given up for the small telescope because of the excellent
18 analogue performance. In the following, we show results just for the far-field receiver since a good system
19 performance at high altitudes has been the main goal of this project. The examples were chosen to show the
20 performance under different conditions such as different levels of background noise and different situations of
21 calibration.

22 **6.1 Water Vapour Measurements up to 20 km**

23 *1 July 2015*

24 The first measurement demonstrating a detection range up to 20 km was achieved on 1 July 2015 (Fig. 12). The
25 polychromator was, still, operated under testing conditions, i.e., just provisionally optically tightened against
26 light from the instrument panels inside the detection compartment to facilitate alignment studies. However, it
27 turned out that the only significant radiation leak was the wide entrance slit of the polychromator (about 40×40
28 mm^2). The strong background of 155 photon counts per hour in 15-m bins is ascribed to scattered radiation from
29 the almost full moon. Despite the resulting noise of ± 25 counts the signal, arithmetically averaged over 52 bins,
30 it stays positive to distances up to 19.7 km (22.4 km a.s.l.).

31 The signal was accumulated over 1 h with a laser pulse energy of just 295 mJ (300 Hz) due to a dirty cell
32 window. The analogue signal was corrected just with a very small exponential correction leaving a slight
33 residual signal undershoot at distances around 12 km that is ascribed to the parallel use of analogue detection and
34 photon counting (Sec. 3.4). The peak analogue signal is about 3 mV, but is rescaled here to match the counting
35 signal. The photon-counting noise corresponds to an analogue voltage of just about ± 15 nV.

36 Water vapour mixing ratios were calculated just by using the analogue data for nitrogen (corrected for a very
37 small exponential wing) because of missing data in the corresponding counting channel during this measurement
38 (Fig. 13). The calibration of the mixing ratio was very difficult since there was macroscopic mutual
39 disagreement of the lidar and all three Vaisala RS 92 radiosonde profiles inspected (Klanner et al., 2017, Fig. 3).

1 A few points below 7 km where the sonde data agree were chosen as reference. The Hohenpeißenberg mixing
2 ratio (early morning) agrees best with the lidar results in the tropopause region and is, therefore, displayed here.
3 The example of 1 July 2015 is special in our test phase: There was very low water vapour around 15.7 km (about
4 2 ppm). The drop is verified by the Hohenpeißenberg profile. Although the sonde data become highly uncertain
5 at higher altitudes we see principal agreement with the lidar. HYSPLIT trajectory calculations indicated
6 advection of tropical air from the Caribbean Sea above the tropopause, slightly downward shifted most likely
7 because of a wrong model orography at the northern rim of the Alps. In the tropics freeze drying in cirrus clouds
8 has been suggested to lead to dehydration and, thus, low humidity (see Sect. 1). Such an inhomogeneity is a
9 strong motivation for lidar work that features a potential for a good time resolution. Water vapour is an excellent
10 tracer for troposphere-to-stratosphere transport (TST) and there is some hope that we can study some cases of
11 TST in the future.

12 *Measurements since 2018*

13 The measurements since 2018 were carried out with full optical insulation of the channels including the cover of
14 the polychromators, with narrow entrance slit and with measurements at 355 nm with the separate Powerlite
15 laser. In 2018 and until 6 February 2019, a total of 14 1-h measurements and several shorter tests were carried
16 out during nights completely without clouds. The minimum H₂O mixing ratios were 4 to 6 ppm, i.e., in the range
17 one would expect for the stratosphere from the literature cited in the introduction.

18 The finally chosen size of the horizontal entrance slit was roughly 4 mm × 8 mm, slightly larger than the
19 minimum that is determined by the product of the large beam divergence of the enlarged laser beam and the
20 focal length of 5 m (receiver). The background signal in 1 h was mostly zero in all 7.5-nm bins (rarely 1 count)
21 except for H₂O. Here, typically 3 to 5 counts were registered. In one case a narrower slit was used (roughly 2
22 mm × 8 mm). This led to 1 to 2 background counts, but also to an indication of a lower backscatter signal. This
23 would be in agreement with the large beam diameter in the focal plane of roughly 2.5 mm as expected from the
24 laser beam divergence and the receiver focal length of 5 m.

25 The reason for the background counts in the water-vapour channel could not be fully clarified. Upper-
26 atmosphere air-glow spectra (Broadfoot et al., 1968; Johnston et al., 1993) show several features in the
27 wavelength range of the in the lidar return for $\lambda \geq 332$ nm. However, some spectral overlap also exists with the
28 components at 332 nm, 353 nm and 355 nm where the background is very low. No clarification has been
29 possible.

30 *19 July 2018*

31 During the early hours of 19 July 2018, two subsequent measurements were made that could be compared. The
32 average laser pulse energy was just 380 mJ (300 Hz). The background count rate was 5-8 counts h⁻¹ bin⁻¹ for a
33 slightly larger entrance slit.

34 The mixing ratios obtained are shown in Fig. 14. The calibration of the first measurement was estimated from
35 the Munich sonde data for the launch at 1:00 CET. The profile for the second measurement looks completely
36 different which, again, demonstrates the strong atmospheric variability of water vapour. Here, the calibration of
37 the lidar mixing ratios was based on the Innsbruck sonde (nominal daily launch: 4:00 CET). We assume that the
38 horizontal homogeneity is much better in the the tropopause region, where we, thus, centred the calibration.
39 However, the agreement is also reasonable around 6.5 km (5 to 10 %).

1 The two profiles for the lidar agree quite well up to about 18 km (Fig. 15), despite the elevated signal
2 background. The second measurement was noisier which is reflected by the larger error bars.
3 It is interesting to note that the sonde data are substantially lower than the mixing ratios from the lidar, which is
4 also the case in the following examples. We speculate that this is due to a change in sonde type from RS 92 to
5 RS 41 by the German Weather Service. We have found that the RS 92 data highly realistic in our tropospheric
6 studies in comparison with our DIAL (Trickl et al., 2014-2016). For 2018, the data for the new sonde type
7 exhibited a positive bias of 2-3 % relative humidity (RH) in intrusion layers.

8 ***5 February 2019: system validation***

9 On 5 and 6 February 2019 several balloons with cryogenic frostpoint hygrometers (CFH; Vömel et al., 2007;
10 2016), standard Vaisala RS-41-SGP radiosondes (Vaisala et al., 2019), ECC ozone sondes (Smit et al., 2007) and
11 COBALD backscatter sondes (Brabec, 2011) were launched in the valley at IMK-IFU (9 km to the north-east of
12 UFS) by a team of the Forschungszentrum Jülich. The data were transmitted to a ground station installed for this
13 campaign at the Zugspitze summit. The combined balloon payload is well tested and regularly also used by the
14 GCOS Reference Upper Air Network (GRUAN) (e.g., Dirksen et al., 2014).

15 The CFH has an uncertainty of about 2-3 % in the troposphere and less than 10 % in the lower stratosphere.
16 Thus, the CFH is especially suitable for measuring water vapour under the dry conditions at the tropopause and
17 in the stratosphere up to altitudes of 28 km.

18 The first night of the campaign was clearer and these results are presented in the following. The conditions for
19 the comparison were excellent: the sondes rose almost vertically up to 8.5 km and then slowly drifted to the
20 south-east (Innsbruck). The balloons stayed within 20 km distance up to the tropopause (12.8 km a.s.l.) and
21 remained within 30 km from IMK-IFU up to 20 km a.s.l.

22 The launch times of the balloons were 18:03 CET (ascent to 16.147 km), 19:03 CET (29.475 km), and 23:00
23 CET (29.469 km). The profiles of the CFH H₂O mixing ratio during that period mutually agreed to within 0.5
24 ppm between 13.0 km and 17.5 km and slightly more up to 26 km. Just two of the three lidar measurements at
25 UFS cover the full standard measurement time of one hour and are presented here.

26 The H₂O Raman backscatter profile for the measurement before midnight is shown in Fig. 16. Due to a narrow
27 slit the H₂O raw data exhibit a background of just 2.33 counts (subtracted here) with a standard deviation of 1.55
28 counts. Two curves with gliding arithmetic means over ± 25 and ± 75 bins are included that suggest a useful range
29 up to $r = 17$ km ($h = 19.7$ km a.s.l.). The remarkably low sensitivity limit for the averaged curve corresponds to
30 roughly 0.1 nV of analogue voltage. The dynamic range within the dry free troposphere and the lower
31 stratosphere covers astonishing seven decades.

32 The nitrogen Raman backscatter signal is considerably larger. Thus, the onset saturation effects can be seen in
33 the photon-counting data below $r = 4$ km. Here, the analogue data are, still, valid for at least two more downward
34 kilometres. The analogue signal starts to deviate from the photon-counting signal due to an exponential decay in
35 the signal processing mentioned in Sect. 3.5. We do not correct this effect because the photon-counting method
36 is used at high altitudes.

37 Figures 17 and 18 show the water vapour mixing ratios obtained for two measurement periods on 5 February
38 with 1-h lidar measurements together with those from the almost simultaneous CFH ascents. In addition, the
39 values for the Munich radiosonde (6 Feb, launched at 1:00 CET) are included for comparison. The grey curve
40 corresponds to the VDI vertical resolution used for the numerical filtering that is about 0.2 km at 14 km and 0.47
41 km at 20 km. Due to the moderate smoothing around 13 km the downward humidity step at 12.8 km is just

1 slightly widened with respect to the CFH sensor. We reduced the vertical resolution of the first measurement
2 around this step by introducing a third-order dependence (polynomial) of the smoothing interval (Eq. 1), but
3 could not improve the steepness of this step. We conclude that the width of the step in the lidar result is primarily
4 determined by the long data acquisition over 1 h.

5 The lidar was calibrated in the upper troposphere above 7.7 km yielding an almost perfect agreement with the
6 CFH measurements in this range. Between 7.7 km and 5.7 km it is, still, satisfactory with deviation of 5 to 10 %.
7 Below this altitude the agreement for the first profile was also acceptable, the lidar value lying in the middle of
8 the CFH mixing ratios for ascent and descent (the latter not shown for clearness). This was quite different for the
9 second profile recorded before midnight when the atmosphere was obviously highly inhomogeneous in space,
10 even on a horizontal scale of 10 km given by the almost vertical rise of the balloon. The presence of several very
11 thin dry layers, also over Munich, indicate a pronounced filamentation.

12 Below this zone the agreement is good for both measurements. This indicates a good cancellation of the overlap
13 functions of the nitrogen and water-vapour channels, similar to DIAL systems.

14 **6.2 Temperature Measurements**

15 *Rotational Method*

16 A few measurements based on the rotational temperature method were evaluated for the near-field receiver
17 (Höveler, 2015). The Cabannes influence was corrected for. A good performance with a temperature noise of
18 less than 1 K in a range up to 8 km in the free troposphere was achieved. With recently purchased new narrow-
19 band interference filters (Materion Barr rejection of Cabannes radiation to 2×10^{-4}) and a better polarizing beam
20 splitter (Laseroptik, $T > 99\%$) we expect a much better rejection of the Cabannes radiation.

21 *Rayleigh Method*

22 Temperature profiles based on the Rayleigh approach have been made for the wavelengths 308 nm, 332 nm, 353
23 nm and, finally, 355 nm. For 308 nm and 332 nm the signals must be corrected for the absorption of the radiation
24 in ozone. The range for 332 nm ends far below the mesosphere and is, therefore, no longer considered. For 308
25 nm a temperature retrieval up to 55 km was achieved. However, the backscatter signal was attenuated with a
26 neutral-density filter by a factor of one thousand in order to avoid detector overload. This means that, without
27 attenuation, a high-speed chopper must be added to cut off the signal returning from the first ten kilometres.
28 Then, the performance could be excellent. The 353-nm channel was successfully tested at low repetition rates
29 (yielding reasonable temperatures up to 52 km), but was given up because of the loss of Raman conversion at
30 full power.

31 Here, we present the first demonstration of a measurement with the separate frequency-tripled Nd:YAG laser
32 (Sect. 2.4) up to the mesosphere on 16 November 2018. This example yields the best example of the technical
33 performance of the UFS lidar: Figure 19 shows the backscatter signals for a 1-h measurement up to as high as
34 120 km. The smoothed combined signal (analogue at low altitudes, photon counting at high altitudes; cyan
35 curve) exhibits low to moderate noise up to 95 km (VDI vertical resolution: black curve). The average photon
36 counting background is considerably less than 1 count. This results in an overall dynamic range of 8 decades.
37 The analogue signal exhibits a considerable distortion at high altitudes which we ascribe of the known (Trickl,
38 2010) magnetic interference of the Nd:YAG laser. Again, a correction is not necessary because the photon-
39 counting data are used at high altitudes.

1 For comparison, we give simulated backscatter profiles calculated from the U.S. Standard Atmosphere and a
2 combination of the 1:00 CET Munich radiosonde and the 13:00 CET NCEP data for our station downloaded
3 from the NDACC web site. The curve for the standard atmosphere (green) is climatological and slightly deviates
4 from the lidar results at high altitudes. It just guides the eye. No deviation of the lidar backscatter profile with
5 respect to the sonde and NCEP data is seen up to end of these data at 53 km (blue curve).
6 The strong near-field signal peak was attenuated by using a narrow aperture and by rotating the laser beam away
7 from the telescope axis. However, this resulted in a slightly reduced overlap as far as almost 20 km, as can be
8 seen in the temperature data (Fig. 20). The combined raw data were smoothed with a VDI vertical resolution
9 scaling as shown in Fig. 19, the maximum value staying below 2 km.
10 The temperature data were initialized at 87 km a.s.l. (density: at 95 km) by using the temperature of the U.S.
11 Standard atmosphere as the start value. The performance is surprisingly good, despite the strongly growing noise
12 of the raw data in this altitude range. The agreement with the temperatures from the Munich radiosonde and
13 NCEP is very good up to the upper end of the NCEP table (50 km) downloaded from the NDACC web site. For
14 higher altitudes we first compared our results with the MSIS model output calculated for our site, as
15 recommended by Wing et al. (2018). There is a strong discrepancy that could not be reduced by selecting the
16 MSIS temperature at 87 km as the start value of the retrieval: The temperature converged to the curve for the
17 standard atmosphere within just 15 km.
18 A comparison with the temperature of the Microwave Limb Sounder (MLS) during the early hours of 16
19 November for a position 3.5° farther to the east. Considering the difference in position the agreement with the
20 MLS temperature profile is quite good, with a strong similarity in structure. The temperature peak at 65 km is
21 present, but slightly downward shifted.
22 In summary we are highly satisfied by this first result for a wide-range temperature measurement. In principle,
23 due to the very small average background signal, Poisson effects in the photon statistics must be taken into
24 consideration. More advanced approaches are needed, such as that presented by Sica and Haeefe (2016).

25 **7 Discussion and Conclusions**

26 The primary goals of the system development described in this paper have been to reduce the measurement time
27 for lower-stratospheric water vapour up to at least 20 km to one hour and to achieve temperature measurements
28 up to more than 80 km. These goals have been met, with a satisfactory performance. Nevertheless, a comparison
29 with the simulations in Sect. 4.4 clearly shows that the measured lidar signal for water vapour is considerably
30 smaller than predicted.

31 At 15 km our measurements typically yield H₂O Raman returns of 2 counts per 7.5-m bin and hour. This is
32 converted to 53 counts for the 200-m bins used in the calculation in Sect. 4.4, one sixth of the 315 counts
33 simulated. Roughly a factor of two is due to the lower laser power in comparison with the 200 W assumed in the
34 simulation. For the rest, apart from uncertainties in the parameters used in the numerical estimate, we found that
35 the most likely reason for this discrepancy is that the Raman cross section used in the calculations is presumably
36 given for the sum of all three ro-vibrational branches. Indeed, the peak signal increased by roughly a factor of
37 three when we removed the 347-nm interference filter, which includes the missing attenuation by the
38 interference filter ($T = 0.72$).

39 As a consequence, we carried out measurements without interference filter. However, this resulted in a much
40 higher stratospheric mixing ratio of 120 ppm due to insufficient blocking of 308- or 332-nm radiation. Thus, for
41 collecting the signal from the entire ro-vibrational band at least a broad-band interference filter (bandwidth 20

1 nm) must be added to reject residual contributions from the other channels and to reduce the observed 3 to 4
2 background counts.

3 The background is dominated by the size of the entrance slit. The optimum slit width is different for both lasers,
4 given different beam divergences. Therefore, in the future two additional slits will be used in focal points of the
5 347-nm and 355-nm channels (Fig. 7). These slits are easier accessible than the entrance slit which facilitates to
6 optimize their position and size.

7 There are obvious possibilities to enhance the laser power. Better transmitting intracavity optics should be
8 installed for significantly reducing the thermal load. A higher transmittance would, therefore, also allow us to
9 remove the cylindrical telescope (Fig. 3) that was introduced to reduce the intracavity intensity on the optical
10 components added by us. As a consequence, the resonator would become shorter and the number of cavity round
11 trips within the fluorescence time of XeCl would grow. As pointed out in Sect. 2.1 the reduction of the numbers
12 of round trips is likely to be the dominant loss factor in the extended resonator.

13 The calibration of the water-vapour channel was confirmed to be a key issue for the long-term operation of the
14 lidar. We hope that the UFS DIAL can soon be re-activated for filling this gap. Additional control by inspecting
15 the data from surrounding radiosonde stations or the signal level at 308 nm and 332 nm are other important tools
16 to ensure long-term stability of the system. A longer comparison with CFH sensors than in the campaign in
17 February 2019 would also be advantageous. This would be particularly important during periods with
18 fluorescing aerosol in the lower stratosphere in order to assess the influence of this kind of background at 347
19 nm.

20 The temperature measurements with a separate, frequency-tripled Nd:YAG laser were quite successful.
21 Improvements could result from using a diode-pumped Nd:YAG laser with 300 or 350 Hz repetition rate,
22 matching that of the XeCl laser. Such lasers are meanwhile available. We expect lower pulse energies for such a
23 laser at 355 nm, but the currently available 160 mJ yielded too much backscatter signal anyway. The remaining
24 efforts will concentrate on testing the rotational Raman channels with the new spectral filters, on implementing
25 the ozone correction (not possible for the configuration with 353 nm) and on completing the remote control of
26 the lidar system. Automatic control of the alignment is the key to more frequent measurements. Lidar
27 measurements at high temporal resolution may yield more information on the role of atmospheric transport, in
28 particular TST, on the water vapour concentration in the UTLS. Finally, we head for long-term operation of the
29 system with stable performance in order to provide insight into the H₂O feedback in the climate system.

30 **5 Data availability**

31 Data can be obtained on request from several authors of this paper (christian.rolf@fzj.de; thomas@trickl.de,
32 hannes.vogelmann@kit.de)

33 **6 Author statement**

34 All authors from Garmisch-Partenkirchen were involved in system development and lidar testing. The Jülich
35 team launched balloons at IMK-IFU.

36 **7 Competing interests**

37 The authors declare that they have no conflict of interest.
38

1 **Acknowledgements**

2 The authors thank Hans Peter Schmid for his interest and support. They are indebted to Werner Funk, Bernd
3 Mielke, Heinz Josef Romanski and Bernhard Stein for numerous important discussions and technical
4 improvements. Stuart McDermid sent valuable information on the feasibility of Raman lidar measurements of
5 H₂O in the stratosphere which encouraged us to start this project. We strongly appreciate the intense discussions
6 with our NDACC colleagues. Wolfgang Steinbrecht generously made available results from the nearby
7 Hohenpeißenberg observatory, Gerald Nedoluha provided the MLS reference data. The good co-operation with
8 the Coherent team in Göttingen was crucial for the laser upgrading. Also crucial has been the excellent help by
9 Werner Moorhoff and Laseroptik who made numerous attempts for optimizing the performance of their
10 dielectric coatings. In particular, their tenacity in optimizing the reflectance of the large mirrors in the transmitter
11 at their own costs this project prevented serious damage to this project. This work has been funded by the
12 Bavarian State Ministry of Environment and Consumer Protection under contracts 45001226 (KIT), TLK01U-
13 49581 and VAO-II TPI/01. KIT acknowledges support of lidar measurements by the European Space Agency
14 (ESA) under Contract 4000123691/18/NL/NF (FIRMOS validation campaign). Balloon profiles utilized in this
15 paper have been provided within the same ESA project by the Forschungszentrum Jülich via subcontract with
16 KIT. The balloon activities were also partly supported by the Helmholtz Association in the framework of
17 MOSES (Modular Observation Solutions for Earth Systems).
18 The service charges for this open-access publication have been covered by a Research Centre of the Helmholtz
19 Association.

20 **References**

- 21 Arshinov, Y. F., Bobrovnikov, S. M., Zuev, V. E., and Mitev, V. M.: Atmospheric temperature measurements
22 using a pure rotational Raman lidar, *Appl. Opt.*, 22, 2984-2990, 1983.
- 23 Avila, G., Fernandez, J. M., Tejada, G., and Montero, S.: The Raman spectra and cross-sections of H₂O D₂O,
24 and HDO in the OH/OD stretching regions, *J. Mol. Spectrosc.*, 228, 38-65, 2004.
- 25 Barnes, J. E., Kaplan, T., Vömel, H., and Read, W. G.: NASA/Aura/Microwave Limb Sounder water vapor
26 validation at Mauna Loa Observatory by Raman lidar, 113, D15S03, doi:10.1029/2007JD008842, 5 pp., 2008.
- 27 Brabec, M.: Backscatter and Humidity Measurements in Cirrus and Dust Clouds using Balloon Sondes, Ph.D.
28 thesis, Eidgenössische Technische Hochschule, Zürich (Switzerland), 96 pp., 2011.
- 29 Bragg, S. L., Brault, J. W., and Smith, W. H.: Line Positions and Strengths in the H₂ Quadrupole Spectrum,
30 *Astrophys. J.*, 263, 999-1004, 1982.
- 31 Broadfoot, A. L., and Kendall, K. R.: The Airglow Spectrum, 3100 – 10,000 Å, *J. Geophys. Res.*, 73, 426-428,
32 1968.
- 33 Carnuth, W., and Trickl, T.: A powerful eyesafe infrared aerosol lidar: application of stimulated Raman
34 backscattering of 1.06 µm radiation, *Rev. Sci. Instrum.*, 65, 3324-3331, 1994.
- 35 Chen, B., and Liu, Z.: Global water vapor variability and trend from the latest 36 year (1979 to 2014) data of
36 ECMWF and NCEP reanalyses, radiosonde, GPS, and microwave satellite, *J. Geophys. Res.*, 121, 11,442–
37 11,462, doi:10.1002/2016JD024917, 2016.
- 38 Congeduti, F., Marengo, F., Baldetti, P., and Vicenti, E.: The multiple lidar '9-eyes', *J. Opt. A*, 1, 185-191, 1999.
- 39 Deuber, B., Kämpfer, N., Feist, D. G.: A New 22-GHz Radiometer for Middle Atmospheric Water Vapor Profile
40 Measurements, *IEEE Transactions on Geoscience and Remote Sensing*, 42, 974-984, 2004.

1 Deuber, B., Haeefe, A., Feist, D. G., Martin, L., Nedoluha, G. E., Yushkov, V., Khaykin, S., Kivi, R., and
2 Vömel, H.: Middle Atmospheric Water Vapour Radiometer (MIAWARA): Validation and first results of the
3 LAPBIAT Upper Tropospheric Lower Stratospheric Water Vapor Validation Project (LAUTLOS-WAVVAP)
4 campaign, *J. Geophys. Res.*, 110, D13306, doi: 10.1029/2004JD005543, 10 pp., 2005.

5 Dickenson, G. D., Niu, M. L., Salumbides, E. J., Komasa, J., Eikema, K. S. E., Pachucki, K., and Ubachs, W.:
6 Fundamental Vibration of Molecular Hydrogen, *Phys. Rev. Lett.*, 110, 193601, 5 pp., 2013.

7 Dionisi, D., Congeduti, F., Liberti, G. L., and Cardillo, F.: Calibration of a Multichannel Water Vapor Raman
8 Lidar through Noncollocated Operational Soundings: Optimization and Characterization of Accuracy and
9 Variability, *J. Atmos. Oceanic Technol.*, 27, 108-121, 2010.

10 Dionisi, D., Liberti, G. L., and Congeduti, F.: Variable Integration Domain technique for Multichannel Raman
11 Water Vapour Lidar Measurements, in: Reviewed and Revised Papers Presented at the 26th International Laser
12 Radar Conference (ILRC 2012), Porto Heli (Greece), A. Papayannis, D. Balis, V. Amiridis, Eds., published in
13 Greece on behalf of the International Co-ordination Group for Laser Atmospheric Studies (ICLAS), 861-864,
14 2012; system description in Ref. 41

15 Dionisi, D., Keckhut, P., Courcoux, Y., Hauchecorne, A., Porteneuve, J., Baray, J. L., Leclair de Bellevue, J.,
16 Vèrèmes, H., Gabarrot, F., Payen, G., Decoupes, R., and Cammas, J. P.: Water vapor observations up to lower
17 stratosphere through the Raman lidar during the Maïdo Lidar Calibration Campaign, *Atmos. Meas. Tech.*, 8,
18 1425-1445, 2015.

19 Dirksen, R. J., Sommer, M., Immler, F. J., Hurst, D. F., Kivi, R., and Vömel, H.: Reference quality upper-air
20 measurements: GRUAN data processing for the Vaisala RS92 radiosonde, *Atmos. Meas. Tech.*, 7, 4463-4490,
21 doi.org/10.5194/amt-7-4463-2014, 2014.

22 Draxler, R., and Hess, G.: An overview of the HYSPLIT_4 modelling system for trajectories, dispersion, and
23 deposition, *Aust. Meteorol. Mag.*, 47, pp. 295-308, 1998.

24 Gettelman, A., Hoor, P., Pan, L. L., Randel, W. L., Hegglin, M. I., and Birner, T.: The Extratropical Upper
25 Troposphere and Lower Stratosphere, *Rev. Geophys.*, 49, RG3003, doi: 10.1029/2011RG000355, 31 pp., 2011.

26 Golubiatnikov, G. Y., and Krupnov, A. F.: Molecular constants of the ground state of oxygen (¹⁶O₂) accounting
27 for new experimental data, *J. Mol. Spectrosc.*, 225, 222-224, 2004.

28 Han, Y., and Westwater, E. R.: Remote Sensing of Tropospheric Water Vapor and Cloud Liquid Water by
29 Integrated Ground-Based Sensors, *J. Atmos. Oceanic Technol.*, 12, 1050-1059, 1995.

30 Hauchecorne, A., and Chanin, M.-L.: Density and Temperature Profiles Obtained by Lidar between 33 and 70
31 km, *Geophys. Res. Lett.*, 7, 565-568, 1980.

32 Hegglin, M. I., Plummer, D. A., Shepherd, T. G., Scinocca, J. F., Anderson, J., Froidevaux, L., Funke, B., Hurst,
33 D., Rozanov, A., Urban, J., von Clarmann, T., Walker, K. A., Wang, H. J., Tegtmeier, S., and Weigel, K.:
34 Vertical structure of stratospheric water vapour trends derived from merged satellite data, *Nature Geoscience*, 7,
35 768-776, 2014.

36 Hints, E. J., Weinstock, E. M., Anderson, J. G., May, R. D., and Hurst, D. F.: On the accuracy of in situ water
37 vapor measurements in the troposphere and lower stratosphere with Harvard Lyman- α hygrometer, *J. Geophys.*
38 *Res.*, 104, 8183-8189, 1999.

39 Hocke, K., and Martin, L.: Monitoring Atmospheric Water Vapour, International Space Science Institute, Bern
40 (Switzerland), ISSI Scientific Reports Series, Vol. 10, Springer (New York, Dordrecht, Heidelberg, London),
41 ISBN 978-1-4614-3908-0, 326 pp., 2013.

1 Höveler, K.: Entwicklung eines Nahbereichsempfängers zur Messung von Wasserdampf- und
2 Temperaturprofilen für das Hochleistungs-Raman-Lidar am Schneefernerhaus, Masterarbeit, Karlsruher Institut
3 für Technologie, Fakultät für Physik, 138 pp., 2015 (in German).

4 Hurst, D. F., Oltmans, S. J., Vömel, H., Rosenlof, K. H., Davis, S. M., Ray, E. A., Hall, E. G., and Jordan, A. F.:
5 Stratospheric water vapor trends over Boulder, Colorado: Analysis of the 30 year Boulder record, *J. Geophys.*
6 *Res.*, 116, D02306, doi: 10.1029/2010JD015065, 12 pp., 2011.

7 Hurst, D. F., Read, W. G., Vömel, H., Selkirk, H. B., Rosenlof, K. H., Davis, S. M., Hall, E. G., Jordan, A. F.,
8 and Oltmans, S. J.: Recent divergences in stratospheric water vapor measurements by frost point hygrometers
9 and the Aura Microwave Limb Sounder, *Atmos. Meas. Tech.*, 9, 4447-4457, 2016.

10 Immler, F., Engelbart, D., and Schrems, O.: Fluorescence from atmospheric aerosol detected by lidar indicates
11 biogenic particles in the lowermost stratosphere, *Atmos. Chem. Phys.*, 5, 345-355, 2005.

12 Jensen, E. J., Ackermann, A. S., and Smith, J. A.: Can overshooting convection dehydrate the tropical
13 tropopause layer? *J. Geophys. Res.*, 112, D11209, doi: 10.1029/2006JD007943, 5 pp., 2007.

14 Johnston, J. E., and Broadfoot, A. L.: Midlatitude Observations of the Night Airglow: Implications to Quenching
15 Near the Mesopause, *J. Geophys. Res.*, 98, 21593-21603, 1993.

16 Kämpfer, N. (Ed.), Smit, H., Kivi, R., Paukkunen, A., Vömel, H., Jeannot, P., Youshkov, V., Nedoluha, G.,
17 Haefele, A., De Wachter, E., Schneider, M., Demoulin, P., Sussmann, R., Notholt, J., Leblanc, T., Trickl, T.,
18 Vogelmann, H., Braathen, G. O., Urban, J., Lambert, J.-C., International Space Science Institute, Bern
19 (Switzerland), ISSI Scientific Reports Series, Vol. 10, ISBN 978-1-4614-3908-0, Springer (Berlin, Heidelberg,
20 New York), 326 pp., 2013.

21 Khattatov, V., Yushkov, V., Kaplanov, M., Zaitzev, I., Rosen, J., and Kjome, N.: Some results of water vapor,
22 ozone and aerosol balloon borne measurements during EASOE, *Geophys. Res. Lett.*, 21, 1299-1302, 1994.

23 Kempfer, U., Carnuth, W., Lotz, R., and Trickl, T.: A wide range ultraviolet lidar system for tropospheric ozone
24 measurements: development and application, *Rev. Sci. Instrum.*, 65, 3145-3164, 1994.

25 Kiehl J. T., and Trenberth, K. E.: Earth's Annual Global Mean Energy Budget, *Bull Am. Met. Soc.*, 78, 197-208,
26 1997.

27 Klanner, L., Trickl, T. and Vogelmann, H.: On the Way to Combined DIAL and Raman-Lidar Sounding of
28 Water Vapour on Mt. Zugspitze – a Progress Report, in: Reviewed and Revised Papers Presented at the 26th
29 International Laser Radar Conference (ILRC 2012), Porto Heli (Greece, 2012), A. Papayannis, D. Balis, V.
30 Amiridis, Eds., published in Greece on behalf of the International Co-ordination Group for Laser Atmospheric
31 Studies (ICLAS), 853-826, 2012.

32 L. Klanner, T. Trickl, H. Vogelmann, Water-vapour measurements up to the lower stratosphere — the high
33 power Raman lidar at the Schneefernerhaus, 28th International Laser Radar Conference, Bucharest (Romania,
34 2017), EPJ Web of Conferences, 176, 01026, DOI: <https://doi.org/10.151/epjconf/201817601026>, 4 pp., 2018.

35 Klett, J. D.: Stable analytical inversion solution for processing lidar returns, *Appl. Opt.*, 20, 211-220, 1981.

36 Klett, J. D.: Lidar inversion with variable backscatter/extinction ratios, *Appl. Opt.*, 24, 1638-1643, 1985.

37 Kley, D., and E. J. Stone, E. J.: Measurement of water vapor in the stratosphere by photodissociation with Ly α
38 (1216 Å) light, *Rev. Sci. Instrum.*, 49, 691-697, 1978.

39 Kneizys, F. X., Anderson, G. P., Shettle, E. P., Gallery, W. O., Abreu, L. W., Selby, J. E. A., Chetwynd, J. H.,
40 and Clough, S. A.: Users guide to LOWTRAN 7, Rep. AFGL-TR-88-0177, Environ. Res. Pap., 1010, 1988.

1 Kreipl, S.: Messung des Aerosoltransports am Alpennordrand mittels Laserradar (Lidar), Dissertation, Friedrich-
2 Alexander-Universität Erlangen-Nürnberg (Germany), 195 pp., 2006; in German.

3 Kung, A.H., Trickl, T., Gershenfeld, N. A., and Lee, Y. T.: State-selective Detection of H₂ by 1 + 1 REMPI via
4 the C ¹Π_u (v' = 0, J') States, *Chem. Phys. Lett.*, 144, 427-430, 1988.

5 Lacis, A. A., Hansen, J. E., Russell, G. L., Oinas, V., and Jonas, J.: The role of long-lived greenhouse gases as
6 principal LW control knob that governs the global surface temperature for past and future climate change, *Tellus*
7 *B*, 65, 19734, doi:10.3402/tellusb.v65i0.19734, 25 pp., 2013.

8 Leblanc, T., and McDermid, I. S.: Accuracy of Raman lidar water vapor calibration and its applicability to long-
9 term measurements, *Appl. Opt.*, 47, 5592-5603, 2008.

10 Leblanc, T., and McDermid, I. S.: Reply to “Comments on “Accuracy of Raman lidar water vapor calibration
11 and its applicability to long-term measurements” ”, *Appl. Opt.*, 50, 2177-2178, 2011.

12 Leblanc, T., McDermid, I. S., and Walsh, T. D.: Ground-based water vapor Raman lidar measurements up to
13 upper troposphere and lower stratosphere for long-term monitoring, *Atmos. Meas. Tech.*, 5, 17-36, 2012.

14 Leblanc, T., Sica, R. J., van Gijssel, J. A. E., Godin-Beekmann, S., Haeefe, A., Trickl, T., Payen, G., and
15 Gabarrot, F.: Proposed standardized definitions for vertical resolution and uncertainty in the NDACC lidar ozone
16 and temperature algorithms. Part 1: Vertical resolution, *Atmos. Meas. Tech.*, 9, 4029-4049, 2016; 18-pp.
17 supplement

18 Luo, B. P., Peter, T., Wernli, H., Fueglistaler, S., Wirth, M., Kiemle, C., Flentje, H., Yushkov, V. A., Khattatov,
19 V., Rudakov, V., Thomas, A., Borrmann, S., Toci, G., Mazzinghi, P., Beuermann, J., Schiller, C., Cairo, F., Di-
20 Donfrancesco, G., Adriani, A., Volk, C. M., Strom, J., Noone, K., Mitev, V., MacKenzie, R. A., Carslaw, K. S.,
21 Trautmann, T., Santacesaria, V., and Stefanutti, L.: Ultrathin Tropical Tropopause Clouds (UTTTCs): II.
22 Stabilization mechanism, *Atmos. Chem. Phys.*, 23, 1083-1091, 2003.

23 McDermid, I. S., Haner, D. A., Kleiman, M. M., Walsh, T. D., and White, M. L.: Differential absorption lidar
24 systems for tropospheric and stratospheric ozone measurements, *Opt. Eng.*, 30, 22-30, 1991.

25 Mieruch, S., Noël, S., Bovensmann, H., and Burrows, J. P.: Analysis of global water vapour trends from satellite
26 measurements in the visible spectral range, *Atmos. Chem. Phys.*, 8, 491–504, 2008.

27 Miloshevich, L. M., Vömel, H., Whiteman, D. N., Lesht, B. M., Schmidlin, F. J., and Russo, F.: Absolute
28 accuracy of water vapor measurements from six operational radiosonde types launched during AWEX-G and
29 implications for AIRS validation, *J. Geophys. Res.*, 111, D09S10, doi: 10.1029/2005JD006083, 25 pp., 2006.

30 Mohr, P. J., Newell, D. B., and Taylor, B. N.: CODATA Recommended Values of the Fundamental Physical
31 Constants: 2014, National Institute of Standards and Technology, Gaithersburg (Maryland, U.S.A.),
32 <https://arxiv.org/pdf/1507.07956.pdf>, 11 pp., 2014.

33 Müller, R., Kunz, A., Hurst, D. F., Rolf, C., Krämer, M., and Riese, M.: The need for accurate long-term
34 measurements of water vapor in the upper troposphere and lower stratosphere with global coverage, *Earth's*
35 *Future*, 4, 25-32, 2016.

36 Nedoluha, G. E., Bevilacqua, R. M., Gomez, R. M., Waltman, W. B., Hicks, B. C., Thacker, D. L., Russell III, J.
37 M., Abrams, M., Pumphrey, H. C., and Connor, B. J.: A comparative study of mesospheric water vapor
38 measurements from the ground-based water vapor millimeter-wave spectrometer and space-based instruments, *J.*
39 *Geophys. Res.*, 102, 16647-16661, 1997.

1 Peter, T., Luo, B. P., Wirth, M., Kiemle, C., Flentje, H., Yushkov, V. A., Khattatov, V., Rudakov, V., Thomas,
2 A., Borrmann, S., Toci, G., Mazzinghi, P., Beuermann, J., Schiller, C., Cairo, F., Di Donfrancesco, G., Adriani,
3 A., Volk, C. M., Strom, J., Noone, K., Mitev, V., MacKenzie, R. A., Carslaw, K. S., Trautmann, T.,
4 Santacesaria, V., and Stefanutti, L.: Ultrathin Tropical Tropopause Clouds (UTTCs): I. Cloud morphology and
5 occurrence, *Atmos. Chem. Phys.*, 23, 1083-1091, 2003.

6 Paltridge, G., Arking, A., and Pook, M.: Trends in middle- and upper-level tropospheric humidity from NCEP
7 reanalysis data, *Theor. Appl. Climatol.*, 98, 351–359, 2009.

8 Pan, L. L., Bowman, K. P., Shapiro, M., Randel, W. J., Gao, R. S., Campos, T., Davis, C., Schauffler, S., Ridley,
9 B. A., Wei, J. C., and Barnett, C.: Chemical behavior of the tropopause observed during the Stratosphere-
10 Troposphere Analyses of Regional Transport experiment, *J. Geophys. Res.*, 112, D18110, doi:
11 10.1029/2007JD008645, 13 pp., 2007.

12 Perrone, M. R., and Piccinno, V.: On the benefits of astigmatic focusing configurations in stimulated Raman
13 scattering processes, *Opt. Comm.*, 133; 534-540, 1997.

14 Reichardt, J., Leinweber, R., and Schwebe, A.: Fluorescing Aerosols and Clouds: Investigations of Co-existence,
15 28th International Laser Radar Conference, Bucharest (Romania, 2017), *EPJ Web of Conferences* **176**, 05010,
16 <https://doi.org/10.1051/epjconf/201817605010>, 4 pp., 2018.

17 Rosenlof, K. H.: How Water Enters the Stratosphere, *Science*, 302, 169-170, 2003.

18 Ross, R.J., and Elliott, W. P.: Radiosonde-Based Northern Hemisphere Tropospheric Water Vapor Trends, *J.*
19 *Climate*, 14, 1602–1612, 2001.

20 Rouillé, G., Millot, G., Saint-Loup, R., and Berger, H.: High-Resolution Stimulated Raman Spectroscopy of O₂,
21 *J. Mol. Spectrosc.*, 154, 372-382, 1992.

22 Scherer, M., Vömel, H., Fueglistaler, S., Oltmans, S. J., and Staehelin, J.: Trends and variability of midlatitude
23 stratospheric water vapour deduced from the re-evaluated Boulder balloon series and HALOE, *Atmos. Chem.*
24 *Phys.*, 8, 1391–1402, 2008.

25 Schmidt, G. A., Ruedy, R. A., Miller, R. L., and Lacis, A. A.: Attribution of the present-day total greenhouse
26 effect, *J. Geophys. Res.*, 115, D20106, doi:10.1029/2010JD014287, 6 pp. 2010.

27 Shibata, T., Kobuchi, M., and Maeda, M.: Measurements of density and temperature profiles in the middle
28 atmosphere with a XeF lidar, *Appl. Opt.*, 25, 685-688, 1986.

29 Sica, R. J., and Haeferle, A.: Retrieval of temperature from a multiple-channel Rayleigh-scatter lidar using an
30 optimal estimation method, *Appl. Opt.*, 54, 1872-1889, 2015.

31 Smit, H. G. J., Straeter, W., Johnson, B. J., Oltmans, S. J., Davies, J., Tarasick, D. W., Hoegger, B., Stubi, R.,
32 Schmidlin, F. J., Northam, T., Thompson, A. M., Witte, J. C., Boyd, I., and Posny, F.: Assessment of the
33 Performance of ECC-ozonesondes under Quasi-flight Conditions in the Environmental Simulation Chamber:
34 Insights from the Jülich Ozone Sonde Intercomparison Experiment (JOSIE), *J. Geophys. Res.*, 112, D19306,
35 doi:10.1029/2006JD007308, 18 pp., 2007.

36 Solheim, F., and Godwin, J. R.: Passive ground-based remote sensing of atmospheric temperature, water vapor,
37 and cloud liquid water profiles by a frequency synthesized microwave radiometer, *Meteorol. Z.*, 7, 370-376,
38 1998.

1 Solomon, S., Rosenlof, K. H., Portmann, R. W., Daniel, J. S., Davis, S. M., Sanford, T. J., and Plattner, G.-K.:
2 Contributions of Stratospheric Water Vapor to Decadal Changes in the Rate of global warming, *Science*, 327,
3 1219-1223, 2010.

4 Stein, A. F., Draxler, R. R., Rolph, G. D., Stunder, B. J. B., Cohen, M. D., and Ngan, F.: NOAA's HYSPLIT
5 atmospheric transport and dispersion modeling system, *Bull. Amer. Meteor. Soc.*, 96, 2059-2077, 2015.

6 Steinbrecht, W., Claude, H., Schönenborn, F., Leiterer, U., Dier, H., and Lanzinger, E., Pressure and
7 Temperature Differences between Vaisala RS80 and RS92 Radiosonde Systems", *J. Atmos. Oceanic Technol.*,
8 25, 909-927, 2008.

9 Stohl, A., and Trickl, T.: A textbook example of long-range transport: Simultaneous observation of ozone
10 maxima of stratospheric and North American origin in the free troposphere over Europe, *J. Geophys. Res.*, 104,
11 30445-30462, 1999.

12 Stohl, A.: A 1-year Lagrangian "climatology" of airstreams in the Northern Hemisphere troposphere and
13 lowermost stratosphere, *J. Geophys. Res.*, 106, 7263-7279, 2001.

14 Stohl, A., Bonasoni, P., Cristofanelli, P., Collins, W., Feichter, J., Frank, A., Forster, C., Gerasopoulos, E.,
15 Gäggeler, H., James, P., Kentarchos, T., Kromp-Kolb, H., Krüger, B., Land, C., Meloen, J., Papayannis, A.,
16 Priller, A., Seibert, P., Sprenger, M., Roelofs, G. J., Scheel, H. E., Schnabel, C., Siegmund, P., Tobler, L., Trickl,
17 T., Wernli, H., Wirth, V., Zanis, P., and Zerefos, C.: Stratosphere-troposphere exchange - a review, and what we
18 have learned from STACCATO, *J. Geophys. Res.*, 108, 8516, doi:10.1029/2002JD002490, STA 1, 15 pp., 2003.

19 Trickl, T.: Upgraded 1.56- μm lidar at IMK-IFU with 0.28 J/pulse", *Appl. Opt.*, 49, 3732-3740, 2010.

20 Trickl, T., and Wanner, J.: The dynamics of the reactions $F + IX \rightarrow IF + X$ ($X = \text{Cl}, \text{Br}, \text{I}$); a laser-induced
21 fluorescence study, *J. Chem. Phys.*, 78, 6091-6101, 1983.

22 Trickl, T., and Wanner, J.: $IF(A \rightarrow X, B \rightarrow X)$ chemiluminescence from the $F + I_2F$ reaction, *J. Chem. Phys.*, 74,
23 6508-6510, 1981; repeated with reduced noise: Trautmann, M., Trickl, T., and Wanner, J.: $IF(A \rightarrow X, B \rightarrow X)$
24 Chemiluminescence of Fluorine-iodide Systems in a Crossed Molecular Beam Experiment, in: "Selectivity in
25 Chemical Reactions", NATO Advanced Science Institute Series, Series C (Mathematical and Physical Sciences),
26 Vol. 245, Proceedings of the NATO Advanced Workshop in Bowes-on-Windermere (Great Britain), Sep. 7 to
27 11, 1987, J. C. Whitehead, Ed., Kluwer Academic Publishers (Dordrecht, The Netherlands), 525-529, 1988;
28 <http://www.trickl.de/NATO1988.pdf>.

29 Trickl, T., Proch, D., and Kompa, K. L.: Resonance-Enhanced 2 + 2 Photon Ionization of Nitrogen: The Lyman-
30 Birge-Hopfield Band System, *J. Mol. Spectrosc.*, 162, 184-229, 1993.

31 Trickl, T., Proch, D., and Kompa, K. L.: The Lyman-Birge-Hopfield System of Nitrogen: Revised Calculation of
32 the Energy Levels, *J. Mol. Spectrosc.*, 171, 374-384, 1995.

33 Trickl, T., Feldmann, H., Kanter, H.-J., Scheel, H. E., Sprenger, M., Stohl, A., and Wernli, H.: Deep
34 stratospheric intrusions over Central Europe: case studies and climatological aspects, *Atmos. Chem. Phys.*, 10,
35 499-524, 2010a.

36 Trickl, T., Kung, A. H., and Lee, Y. T.: A Pulsed Source of Cold Hydrogen and Hydrogen Clusters:
37 Development and Extreme-ultraviolet Studies, *Appl. Phys. B*, 101, 321-335, 2010b; the detection sensitivity for
38 H_2 was enhanced by orders of magnitude with respect to the $1.7 \times 10^5 \text{ cm}^{-3}$ of Kung et al. (1988).

39 Trickl, T., Giehl, H., Jäger, H., and Vogelmann, H.: 35 years of stratospheric aerosol measurements at Garmisch-
40 Partenkirchen: from Fuego to Eyjafjallajökull, and beyond, *Atmos. Chem. Phys.*, 13, 5205-5225, 2013.

1 Trickl, T., Vogelmann, H., Giehl, H., Scheel, H. E., Sprenger, M., and Stohl, A.: How stratospheric are deep
2 stratospheric intrusions? *Atmos. Chem. Phys.*, 14, 9941-9961, 2014.

3 Trickl, T., Vogelmann, H., Flentje, H., and Ries, L.: Stratospheric ozone in boreal fire plumes – the 2013 smoke
4 season over Central Europe, *Atmos. Chem. Phys.*, 15, 9631-9649, 2015.

5 Trickl, T., Vogelmann, H., Fix, A., Schäfler, A., Wirth, M., Calpini, B., Levrat, G., Romanens, G., Apituley, A.,
6 Wilson, K. M., Begbie, R., Reichardt, J., Vömel, H. and Sprenger, M.: How stratospheric are deep stratospheric
7 intrusions into the troposphere? LUAMI 2008, *Atmos. Chem. Phys.*, 16, 8791-8815, 2016.

8 Trickl, T., Vogelmann, H., Ries, L., and Sprenger, M.: Very high stratospheric influence observed in the free
9 troposphere over the Northern Alps – just a local phenomenon? *Atmos. Chem. Phys.*, 20, 243-266, 2020a.

10 Trickl, T., Neidl, F., Giehl, H., Perfahl, M., and Vogelmann, H.: Three decades of tropospheric ozone lidar
11 development at Garmisch-Partenkirchen, *Atmos. Meas. Tech.*, AMT-2020-89, in press, 2020b.

12 U.S. Standard Atmosphere 1976, National Oceanic and Atmospheric Organization (NOAA), National
13 Aeronautics and Space Administration, United States Air Force, NOAA-S/T 76-1562, U.S. Printing Office
14 (Washington, D.C.), 227 pp., 1976.

15 Vaisala: Vaisala Radiosonde RS41 Measurement Performance, White Paper, Vaisala, Helsinki (Finland),
16 [https://www.vaisala.com/sites/default/files/documents/WEA-MET-RS41-Performance-White-paper-](https://www.vaisala.com/sites/default/files/documents/WEA-MET-RS41-Performance-White-paper-B211356EN-B-LOW-v3.pdf)
17 [B211356EN-B-LOW-v3.pdf](https://www.vaisala.com/sites/default/files/documents/WEA-MET-RS41-Performance-White-paper-B211356EN-B-LOW-v3.pdf), 28 pp., 2017.

18 VDI guide line 4210, Remote sensing, Atmospheric measurements with LIDAR, Measuring gaseous air
19 pollution with the DAS LIDAR, Verein Deutscher Ingenieure (Düsseldorf, Germany), pp. 47, 1999.

20 Vérèmes, H., Payen, G., Keckhut, P., Dufлот, V., Baray, J.-L., Cammas, J.-P., Evan, S., Posny, F., Körner, S.,
21 and Bosser, P.: Validation of the Water Vapor Profiles of the Raman Lidar at the Maïdo Observatory (Reunion
22 Island) Calibrated with Global Navigation Satellite System Integrated Water Vapor, *Atmosphere*, 10, 713,
23 doi:10.3390/atmos10110713, 21 pp., 2019.

24 Vömel, H., Selkirk, H., Miloshevich, L., Valverde-Canossa, J., Valdés, J., Kyro, E., Kivi, R., Stolz, W., Peng,
25 G., and Diaz, J. A., Radiation Dry Bias of the Vaisala RS92 Humidity Sensor, *J. Atmos. Oceanic Technol.*, 24,
26 953-963, 2007a.

27 Vömel, H., David, D. E., and Smith, K.: Accuracy of tropospheric and stratospheric water vapor measurements
28 by the cryogenic frost point hygrometer: Instrumental details and observations, *J. Geophys. Res.*, 112, D08305,
29 doi: 10.1029/2006JD007224, 14 pp., 2007b.

30 Vömel, H., Naebert, T., Dirksen, R., and Sommer, M.: An update on the uncertainties of water vapor
31 measurements using Cryogenic Frostpoint Hygrometers, *Atmos. Meas. Tech.*, 9, 3755-3768, 2016.

32 Vogelmann, H., and Trickl, T.: Wide-range sounding of free-tropospheric water vapor with a differential-
33 absorption lidar (DIAL) at a high-altitude station, *Appl. Opt.*, 47, 2116-2132, 2008.

34 Vogelmann, H., Sussmann, R., Trickl, T., and Borsdorff, T.: Intercomparison of atmospheric water vapor
35 soundings from the differential absorption lidar (DIAL) and the solar FTIR system on Mt. Zugspitze, *Atmos.*
36 *Meas. Tech.*, 4, 835-841, 2011.

37 Vogelmann, H., Sussmann, R., Trickl, T., and Reichardt, A.: Spatiotemporal variability of water vapor
38 investigated using lidar and FTIR vertical soundings above the Zugspitze, *Atmos. Chem. Phys.*, 14, 3135-3148,
39 2015.

1 Weinstock, E. M., Schwab, J. J., Nee, J. B., Schwab, M. J., and Anderson, J. G.: A cryogenically cooled
2 photofragment fluorescence instrument for measuring stratospheric water vapor”, *Rev. Sci. Instrum.*, 61, 1413-
3 1432, 1990.

4 Westwater, E. R.: The accuracy of water vapor and cloud liquid determination by dual-frequency ground-based
5 microwave radiometry”, *Radio Sci.*, 13, 677-685, 1978.

6 Whiteman, D. N., Rush, K., Rabenhorst, S., Welch, W., Cadirola, M., McIntire, G., Russo, F., Adam, M.,
7 Venable, D., Connell, R., Veselovski, I., Forno, R., Mielke, B., Stein, B., Leblanc, T., McDermid, S., and
8 Vömel, H.: Airborne and Ground-based measurements using a High-Performance Raman Lidar, *J. Atmos.*
9 *Ocean. Technol.*, 27, 1781–1801, 2010.

10 Whiteman, D. N., Venable, D., and Landulfo, E.: Comments on “Accuracy of Raman lidar water vapor
11 calibration and its applicability to long-term measurements”, *Appl. Opt.*, 50, 2170-2176, 2011.

12 Wing, R., Hauchecorne, A., Keckhut, P., Godin-Beekmann, S., Khaykin, S., McCullough, E. M., Mariscal, J.-F.
13 and d’Almeida, E.: Lidar temperature series in the middle atmosphere as a reference data set – Part 1: Improved
14 retrievals and a 20-year cross-validation of two co-located French lidars, *Atmos. Meas. Tech.*, 11, 5531–5547,
15 2018.

16 Yoshino, K., Esmond, J. R., Parkinson, W. H., Ito, K., and Matsui, T.: Absorption cross section measurements of
17 water vapor in the wavelength region 120 to 188 nm, *Chem. Phys.*, 211, 387-391, 1996; erratum: *Chem. Phys.*,
18 215, 429-430, 1997.

19 Zahn, A., Christner, E., van Velthoven, P. F. J., Rauthe-Schöch, A., and Brenninkmeijer, C. A. M.: Processes
20 controlling water vapor in the upper troposphere/lowermost stratosphere: An analysis of 8 years of monthly
21 measurements by the IAGOS-CARIBIC observatory, *J. Geophys. Res.*, 119, 11505-11525, doi:
22 10.1002/2014JD021687, 2014.

23 Zöger, M., Afchine, A., Eicke, N., Gerhards, M.-T., Klein, E., McKenna, D. S., Mörschel, U., Schmidt, U., Tan,
24 V., Tuijter, F., Woyke, T., and Schiller, C.: Fast in situ stratospheric hygrometers: A new family of balloon-
25 borne and airborne Lyman- α photofragment fluorescence hygrometers, *J. Geophys. Res.*, 104, 1807-1816, 1999.

26

1 **Table 1. Transmitter details**

2	Laser source	XeCl laser (Coherent, model Lambda SX)
3	Laser wavelength	307.955 nm
4	Maximum power (at 2.0 kV)	420 W
5	Stabilized power (all lines)	350 W
6	Single-line power	180 W
7	Line width	0.036 nm
8	Optimum spectral purity	99.5 %
9	Linear polarization	99.6 %
10	Pulse repetition rate	350 s ⁻¹
11	Raman shifted wavelength	353.144 nm
12	Maximum Raman conversion effi-	
13	ciency (f = 2.0 m, 40 bar, 350 s ⁻¹)	5 % with distorted alignment, otherwise 0 %
14	Second laser (starting 2018)	Nd:YAG (Continuum, model PL8020 Precision)
15	Wavelength	354.8123 nm (injection-seeded)
16	Pulse energy	160 mJ at 20 Hz repetition rate
17	Final beam expansion (f = 1.75 m)	5.7:1
18	Final beam dimensions	0.20×0.20 m ²
19	Final beam divergence	≤ 0.5 mrad
20		
21		

1	Table 2: Receiver details	
2	Primary mirrors	0.13 m diameter, $f = 0.72$ m
3		0.50 m diameter, $f = 2.0$ m
4	Field of view	large telescope: about 0.8×0.2 mrad ²
5	Detection wavelengths:	306.791 nm, 307.390 nm, 307.355 nm, 331.751 nm, 346.978 nm,
6		353.144 nm, 354.812336 nm ^a
7	Raman shifts:	Vibrational Q branch of H ₂ O ^b : 3652 cm ⁻¹ (centre of the stronger lines. Range
8		of Q-branch: 3628 to 3658 cm ⁻¹ ($\Delta\lambda = 0.36$ -nm)
9		nitrogen, Q ₆ line (population peak) ^c : 2329.1821 cm ⁻¹
10		N ₂ and O ₂ rotational shifts: taken from references in footnotes c and d
11		hydrogen, Q ₁ line ^c : 4155.2521 cm ⁻¹
12	Wavelength separation	polarization-sensitive beam splitters and interference filters
13		($\Delta\lambda = 0.75$ nm f.w.h.m. for H ₂ O, 0.25 nm otherwise)
14	PMTs	Hamamatsu R7400U-03, modified by RSV
15	Pre-amplifiers	Analog Modules, gain 1–10, bandwidth 4 MHz, sometimes used for H ₂ O
16	Transient digitizers	Licel, 6 units, 12 bit, 20 MHz, ground-free input stages
17	Photon counting	FAST ComTec, 100 ps time bins, 7.5-m detection bins
18		
19	(a)	Measured during the project described by Vogelmann and Trickl (2008)
20	(b)	Avila et al., 2004
21	(c)	Trickl et al., 1993; 1995
22	(d)	Rouillé, 1992; Golubiatnikov and Krupnov, 2004
23	(e)	Bragg et al., 1982; Dickensen et al., 2013
24		
25		

1 **Table 3: Specifications of the polychromator optics**

2 **Broadband optics**

3 Component	4 Diameter	5 Focal Length	6 or Wavelength	7 Comments
8 f_1 lenses	75 mm	150 mm		
9 f_2 lenses	15 mm	17 mm		large telescope
	15 mm	30 mm		small telescope
10 45°-high reflectors	75 mm	all wavelengths		S and P polarization
11 45°-beam splitter 1	75 mm	308 nm		T = 99 % P (308 nm), T = 99-100 % P (> 325 nm)
				T = 94 % S (355 nm)
				R ≈ 99.8 % S (308 nm)
12 45°-beam splitter 2	75 mm	308 nm		T = 63 % S, R = 37 % S
13 45°-beam splitter 3	75 mm	308 nm		R = 100 % P (308 nm)
				T = 83 % P (332 nm)
				T ≈ 90 % P (347, 355 nm)
14 45°-beam splitter 4	75 mm	355 nm		T = 99 % P (332, 347 nm)
				R ≈ 99.8 % S (355 nm)
15 45°-beam splitter 5	75 mm	332 nm		R = 99.8 % P,
				T > 99 % P (347, 355 nm)
16 45°-beam splitter 6 ^{*)}	75 mm	347 nm		R = 84 % P
				T = 99.3 % P (353 nm)

17 ^{*)} No longer used since 2018, not shown in Fig. 9

18 **Narrow-band interference filters**

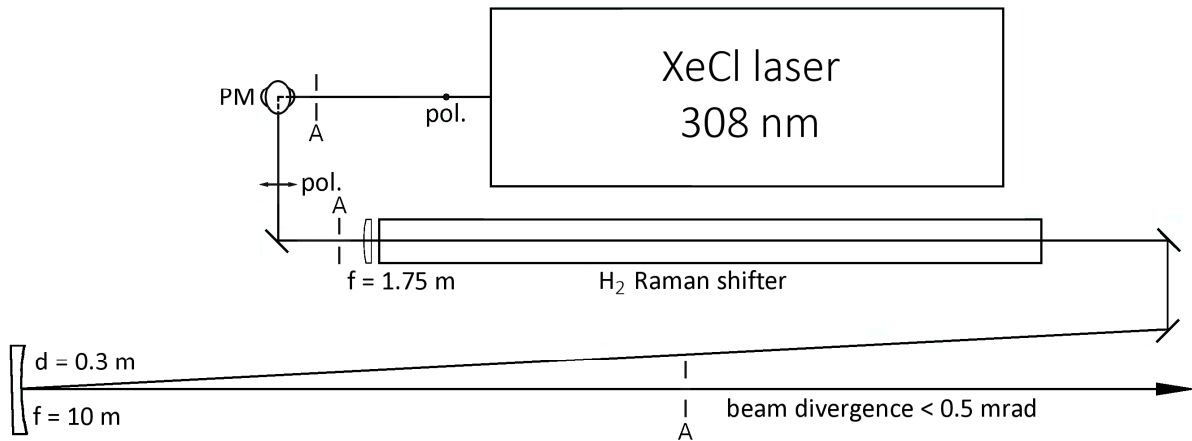
19 Wavelength	20 Bandwidth	21 Maximum T	22 Maximum T	23 Producer
24 [nm]	25 [nm]	26 (large telescope)	27 (small telescope)	
28 306.791	0.25	25 %	25 %	Materion Barr
29 307.390	0.15	27 %	25 %	Materion Barr
30 307.955	0.25	35 %	32 %	Materion Barr
31 331.751	0.25	52 %	43 %	Materion Barr
32 346.978	0.75	74 %	62 %	Materion Barr
33 353.144	0.25	43 %	34 %	Materion Barr
34 354.812	< 1.2	> 80 %		Alluxa

35 All diameters 50 mm

36
37

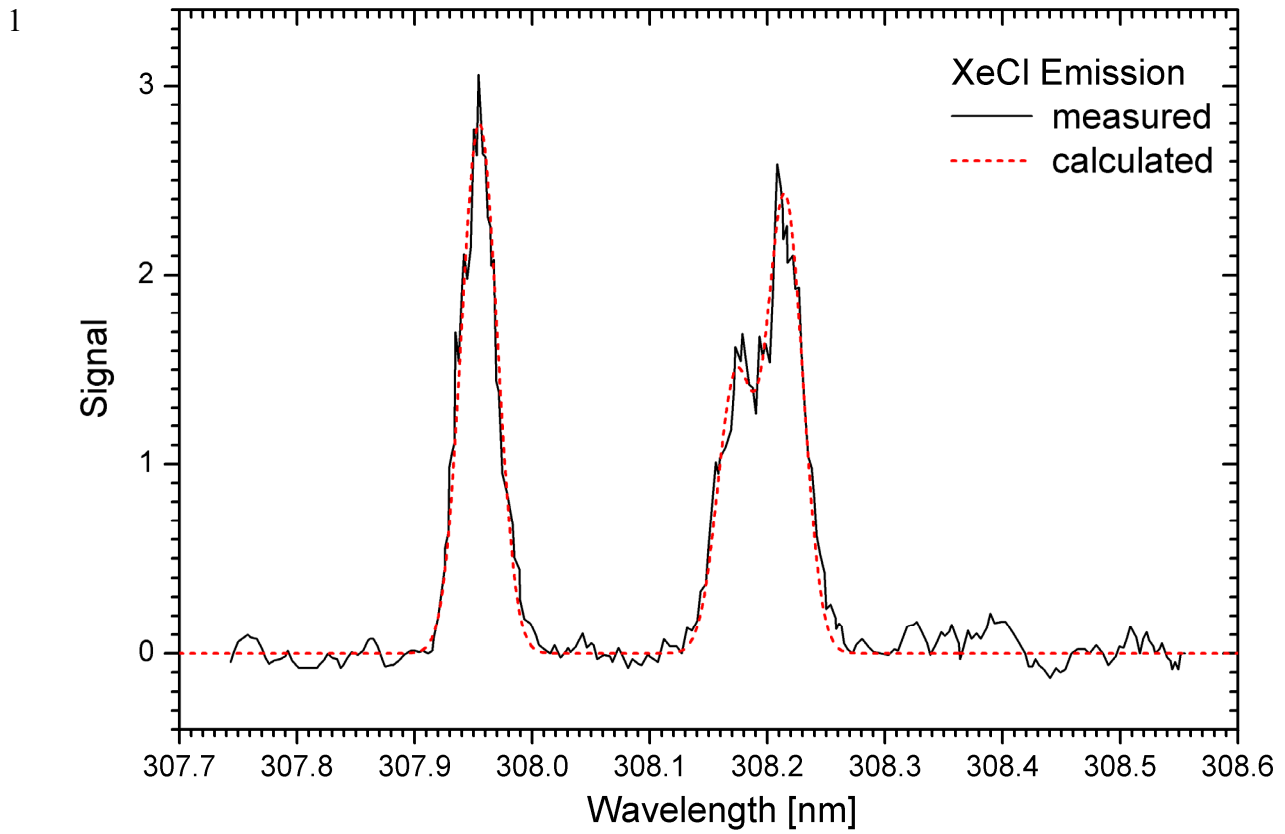
1 **Figures:**

2



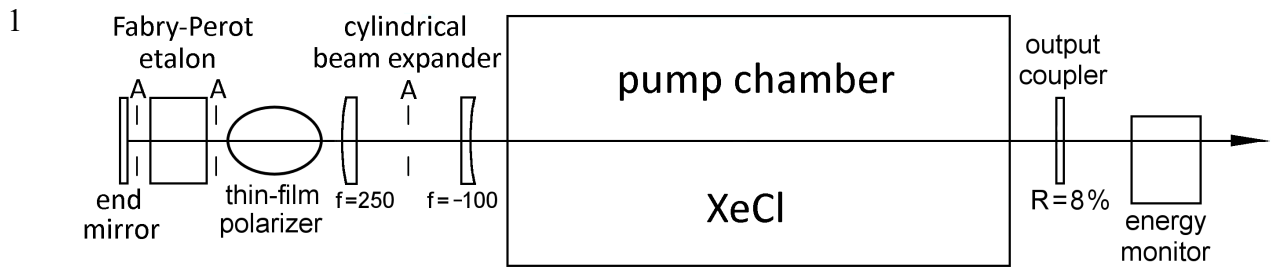
3 **Fig. 1.** Overview of the transmitter part of the UFS Raman lidar: The laser beam profile is expanded to a 36×36 -
4 mm^2 square shape by a $f = -100 \text{ mm} - f = 250 \text{ mm}$ pair of cylindrical lenses (recently removed), sent down by a
5 combination of two plane mirrors (rotating the polarization by 90°) before it is focussed into a vacuum cell
6 (originally Raman shifter) 3.6 m long with a $f = 1.75 \text{ m}$ lens (initially $f = 2.0 \text{ m}$). The beam diverges from the
7 focal point is collimated by an $f = 10 \text{ m}$ concave mirror and reaches the motorized beam-steering mirror in a
8 vertical exit shaft outside the laboratory (not shown). Three apertures allow to control the beam pointing.

9



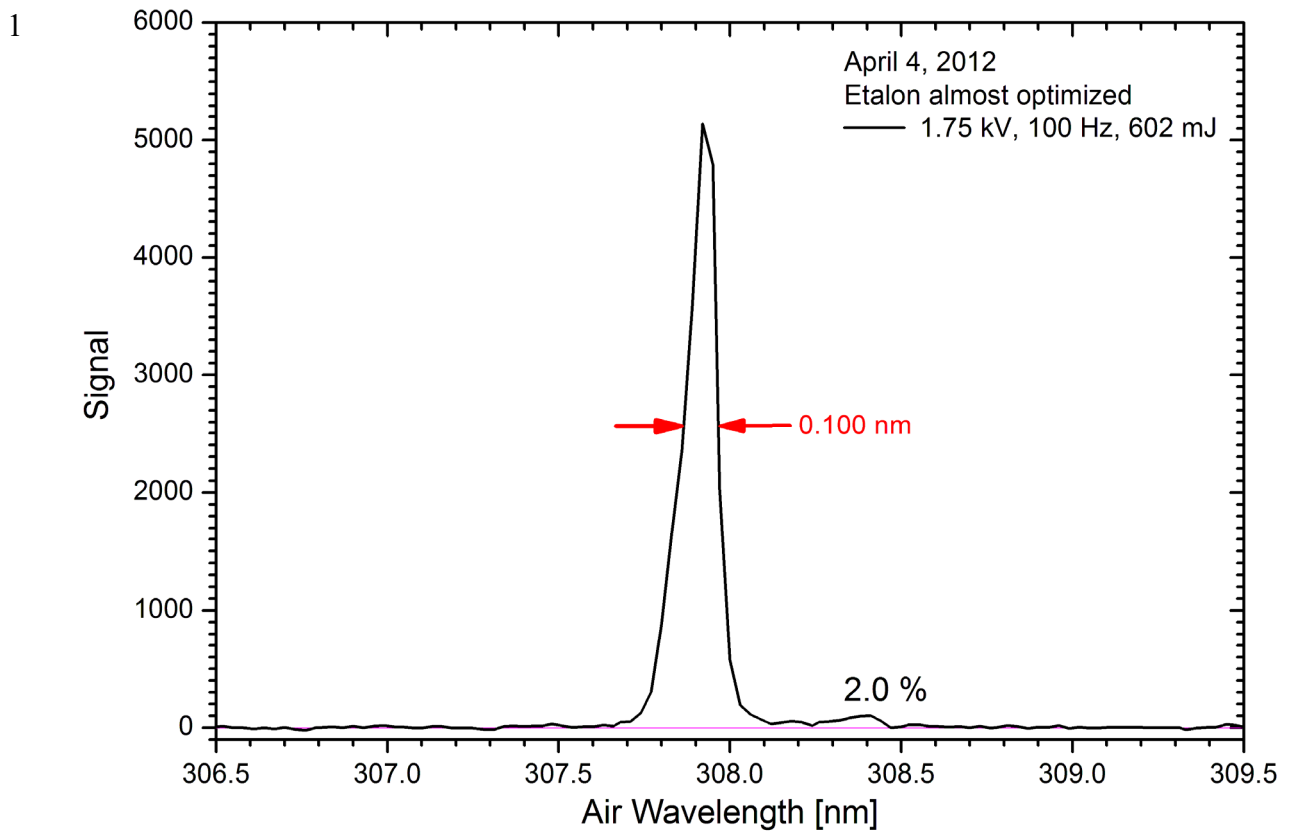
2 **Fig. 2.** Emission spectrum of a Coherent high-power XeCl laser in broadband operation (source: Coherent); the
3 dashed red curve is the sum of three Gaussian lines with centres at 308.955 nm, 308.173 nm and 308.215 nm and
4 full width at half maximum of 0.0357 nm.

5



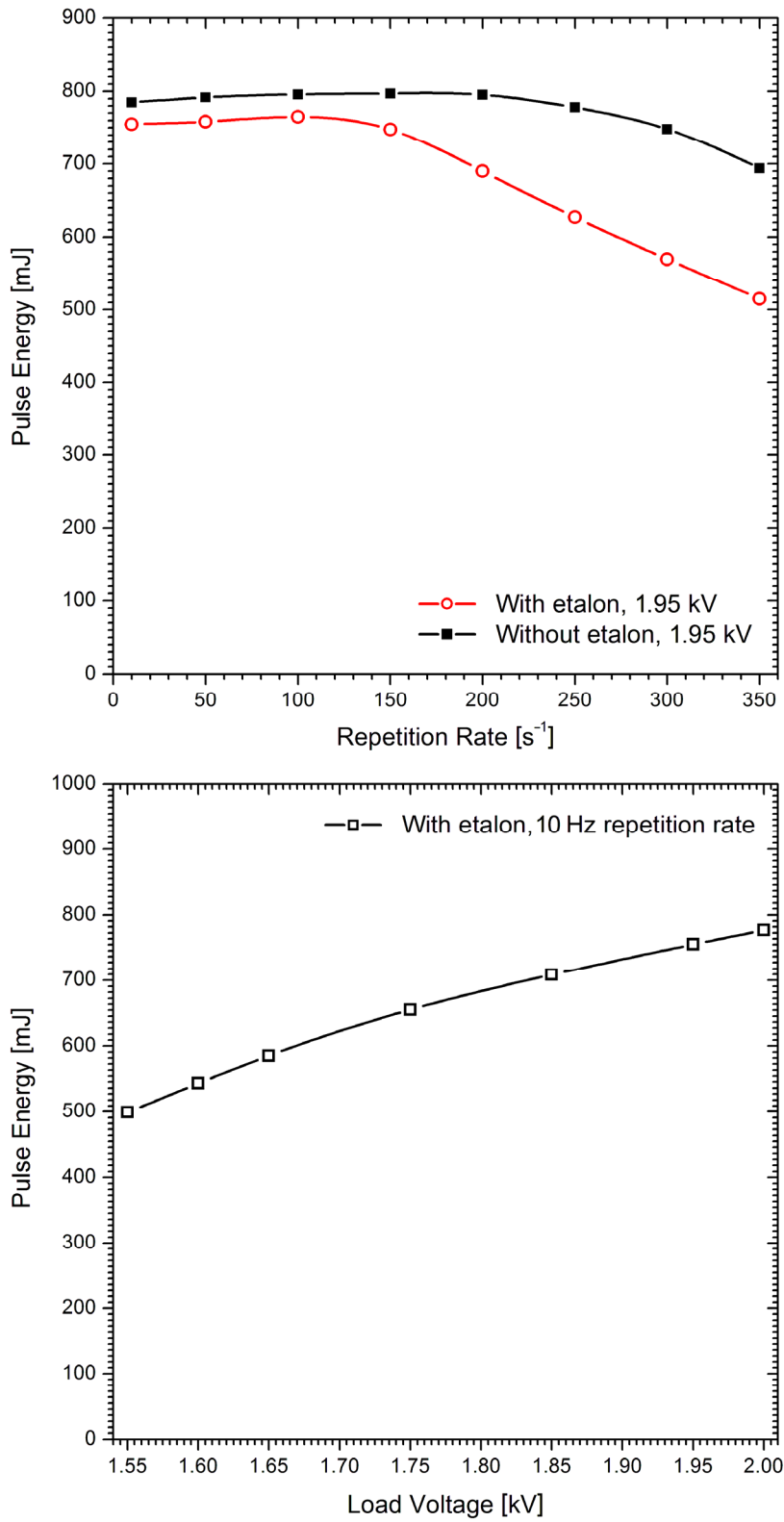
2 **Fig. 3.** Top view of the modified Lambda SX laser system; $36 \times 36\text{-mm}^2$ square apertures (A) are used for
 3 protecting optical components from potential powerful reflections from accidentally rotated components. The
 4 polarizer is oriented out of plane at Brewster's angle.

5
6



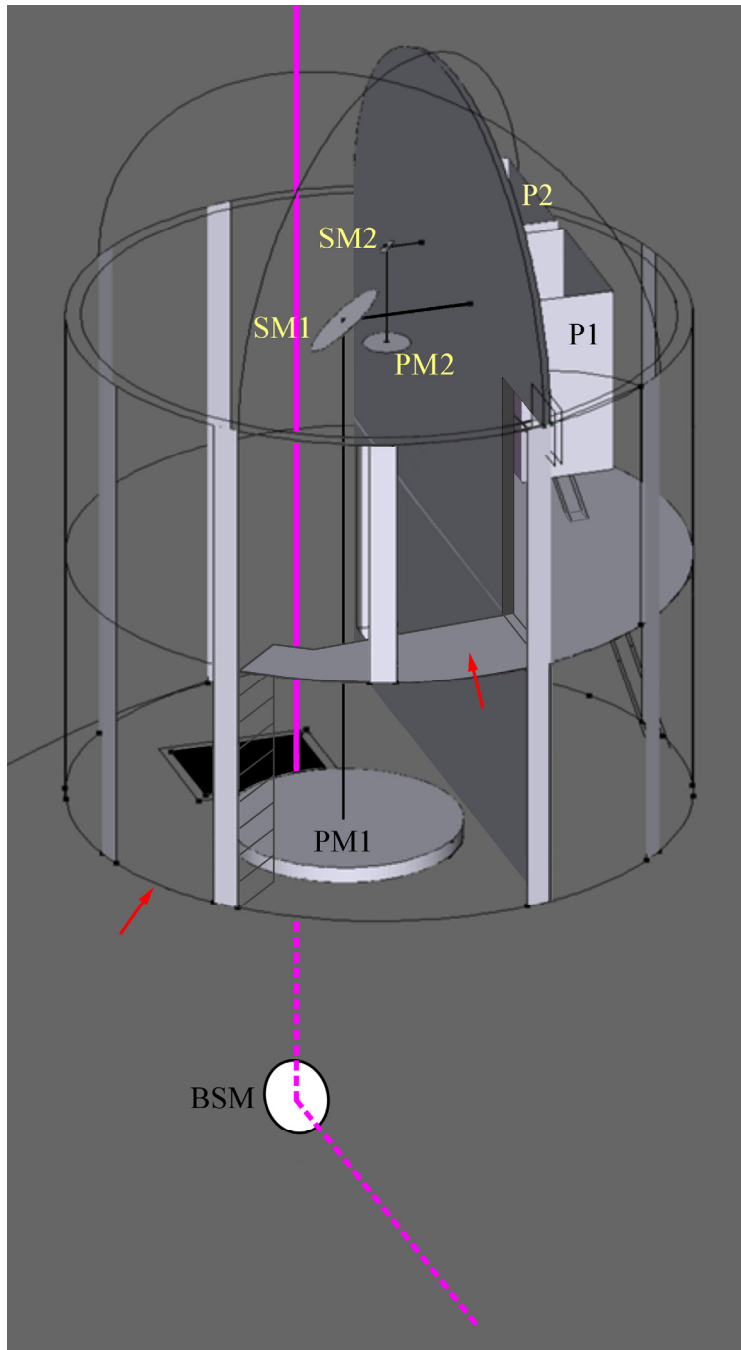
2 **Fig. 4.** Spectrum of the laser emission with almost optimized etalon angle; the laser was operated with 10 Hz
3 repetition rate, 1.75 kV load voltage and 663 mJ (including the polarizer).
4

1



2 **Fig. 5.** Optimized pulse energy as a function of the repetition rate (top) and load voltage (bottom); for
3 comparison: The maximum pulse energy of the broadband laser as delivered is 1.25 J (at 2.0 kV and 300 Hz).
4

1



2 **Fig. 6.** Receiver tower mounted on the terrace above the lidar laboratory: The tower is covered by a 4.2-m-
3 diameter astronomical dome with a 1.5-m slit: The laser beam (violet) emerges from a former emergency shaft.
4 The plane formed by the axes of the large telescope and the laser beam contains the section of the laser beam in
5 the lower floor. This plane is perpendicular to the plane formed by the axes of the small telescope and the laser
6 beam. Abbreviations:

7 BSM beam-steering mirror

8 PM: primary mirror

9 SM: secondary mirror

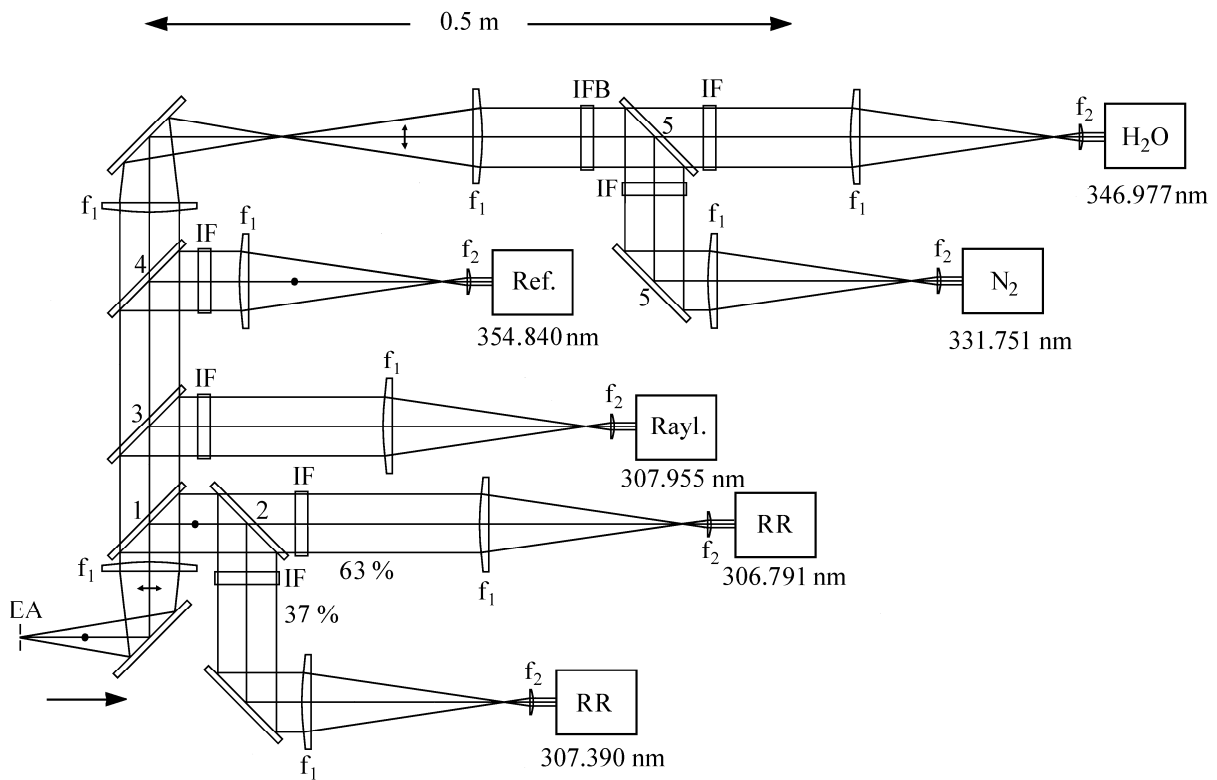
10 P: Polychromator

11 1, 2: belonging to far-field receiver, near-field-receiver, respectively

12 The two red arrows indicate the two entrances of the tower.

13

1



2 **Fig. 7.** Final polychromator design: The true orientation of the mounting plate (vertical) is rotated clockwise by
 3 90°. The radiation cone from the telescopes (arrow) enters the polychromators from behind the plate as indicated
 4 by the polarization dot next to the arrow. In detail:

5 EA: Entrance aperture with four adjustable blades (OWIS)

6 1: Beam splitter transmitting almost all P-polarized radiation (308-355 nm) and highly reflects the S-
 7 polarized 308-nm radiation (Laseroptik)

8 2: 63 %/37 % beam splitter for S-polarized 308-nm radiation (Laseroptik)

9 3: Beam splitter reflecting all radiation at 308 nm and transmitting 83-91 % of the longer-wavelength P
 10 components (Laseroptik)

11 4: Polarizing beam splitter (Laseroptik)

12 5: Sharp-edged long-pass filter for P polarization reflecting about 99 % at 332 nm and transmitting 99 %
 13 of the longer-wavelength components (Materion-Barr)

14 IF: Interference filters with bandwidths of 0.25 nm except for 307.39 nm (0.15 nm) and 347 nm (0.75 nm)
 15 (Materion Barr, Alluxa)

16 IFB: Broadband interference filter transmitting between 330 and 355 nm with $T = 85-90\%$ and blocking the
 17 radiation outside this range by at least 10^5 (Semrock).

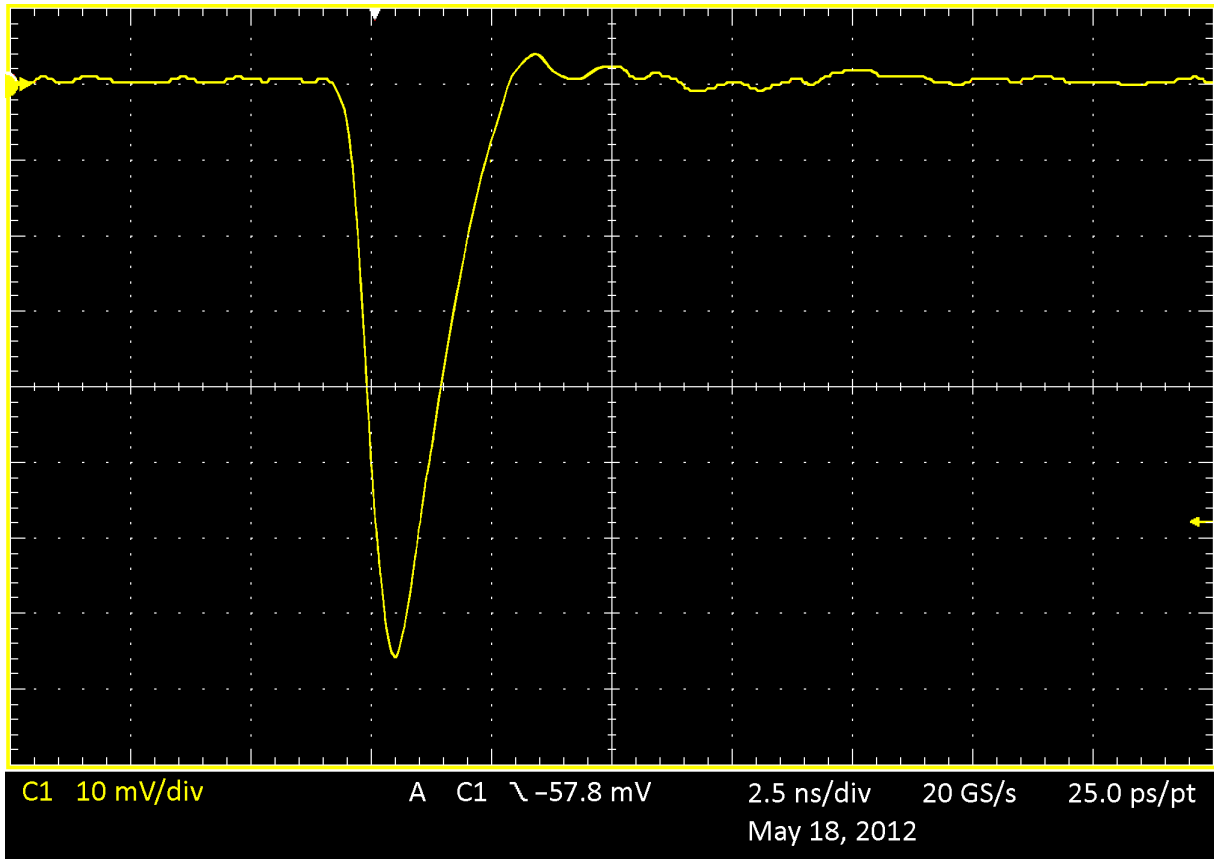
18 Lenses: $f_1 = 150$ mm and $f_2 = 18$ mm (large telescope), $f_2 = 30$ mm (small telescope)

19 Detailed specifications: Table 3

20

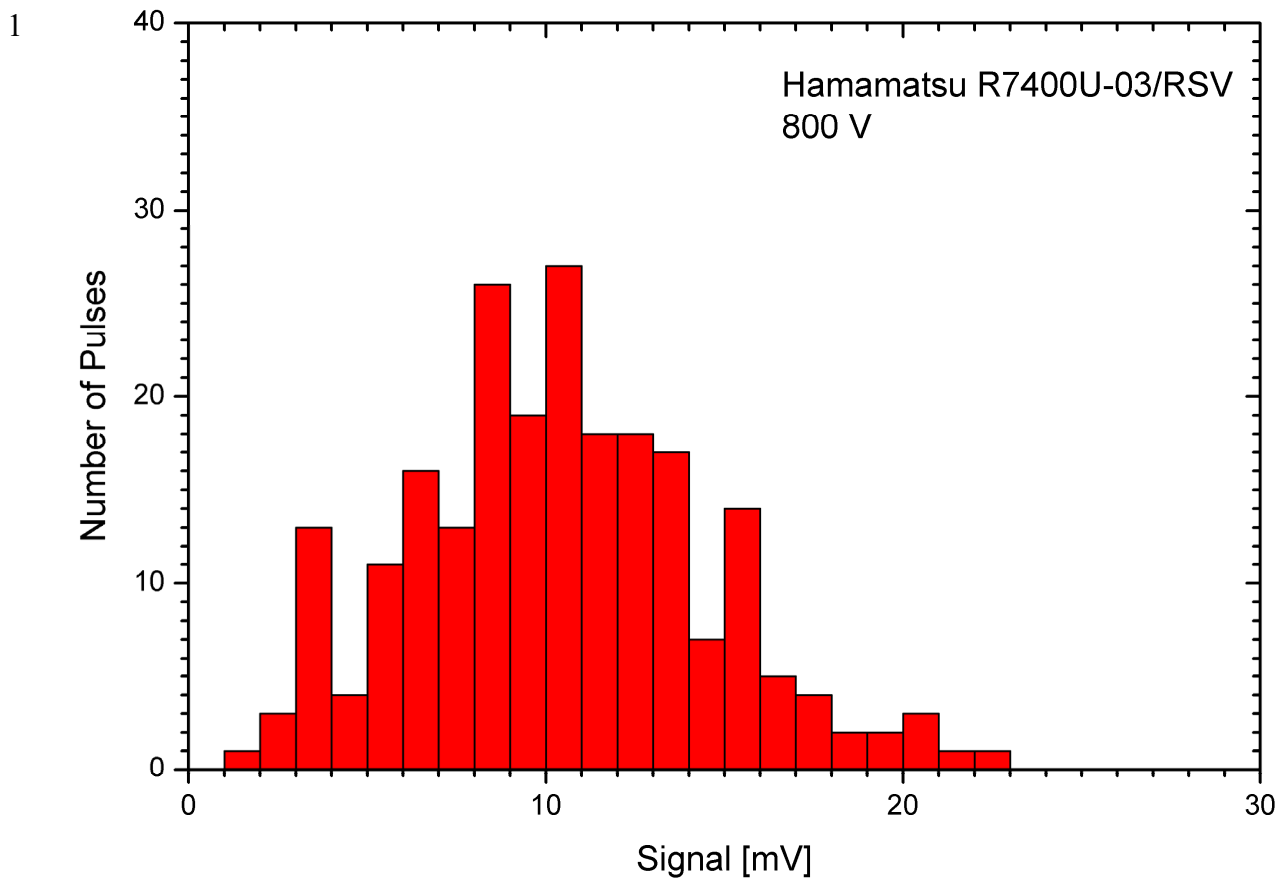
21

1



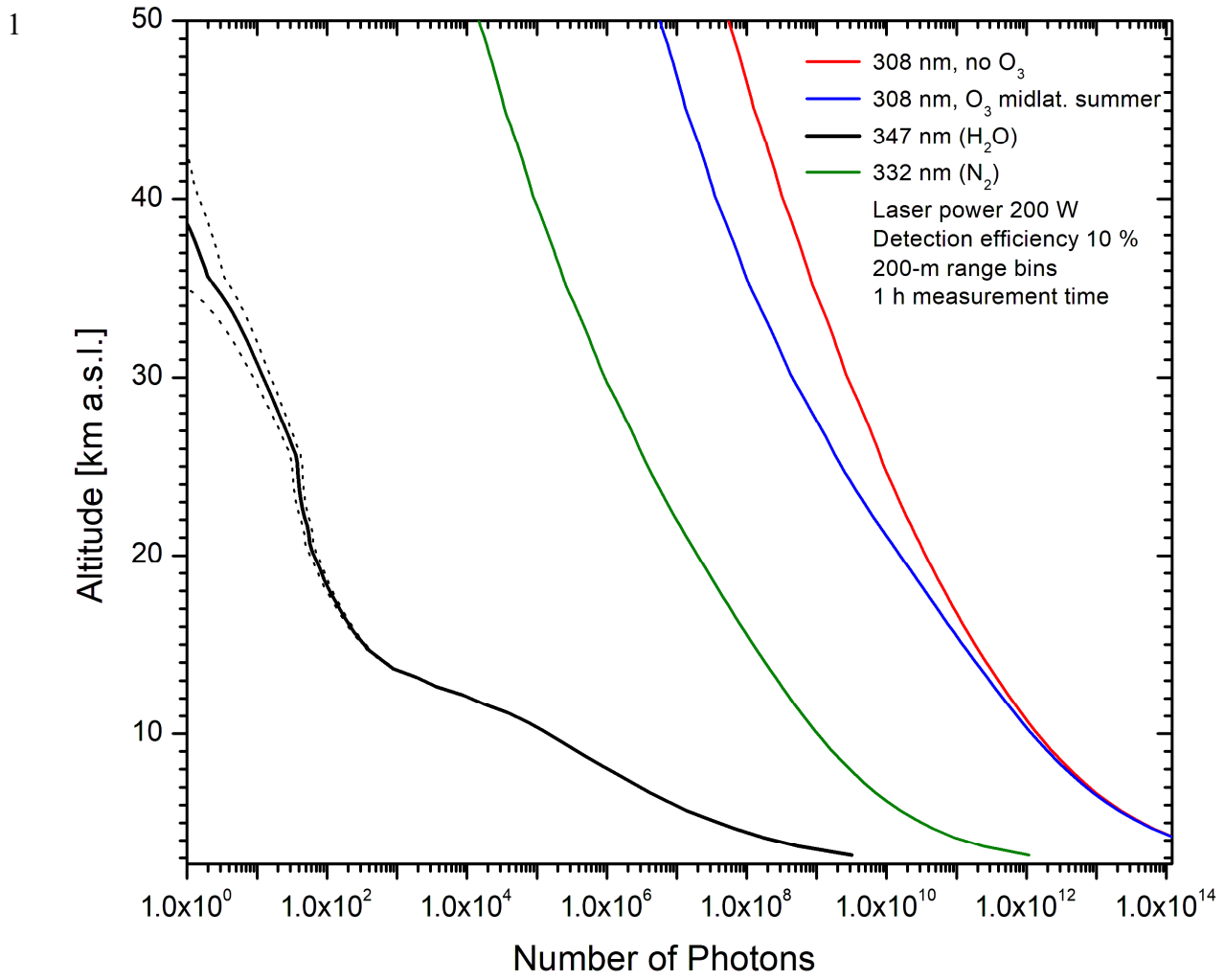
2 **Fig. 8.** Single-photon pulse from a Hamamatsu R7400P-03 PMT with the most recent version of the Romanski
3 (RSV) socket, measured with a 1-GHz digital oscilloscope (Tektronix, DPO 7104); from (Trickl et al., 2020b)

4

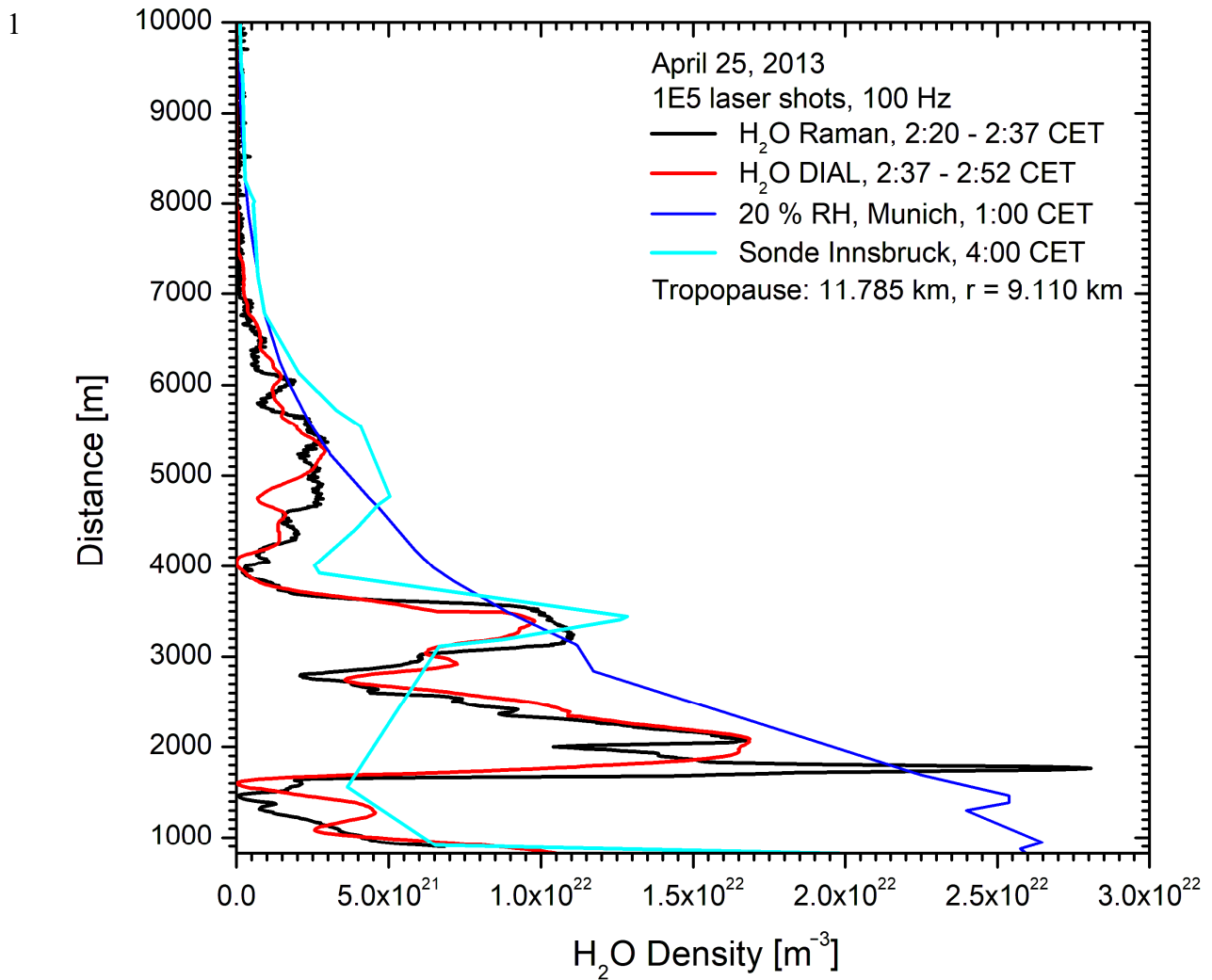


2 **Fig. 9.** Pulse height distribution of a Hamamatsu R7400-03 PMT (RSV module) for 800 V of operating voltage
3 determined from a long time scan with a 1-GHz digital oscilloscope (sign of the pulse amplitudes inverted); from
4 (Trickl, 2020b).

5

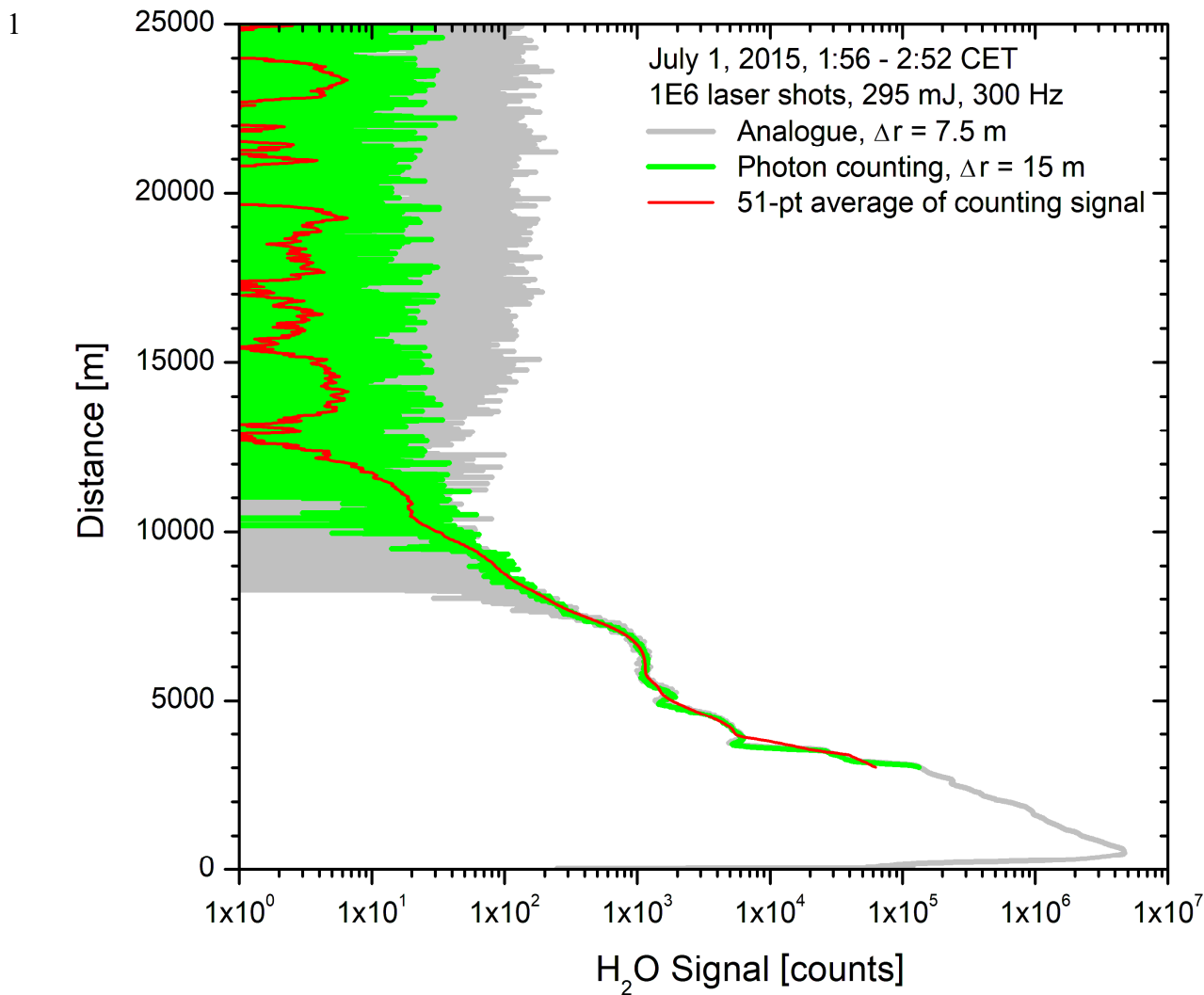


2 **Fig. 10.** Simulations of the backscatter signals for four wavelengths specified in the upper right corner; An
 3 average laser power at 308 nm of 200 W, a detection efficiency of 10 %, a range bin of 200 m and a
 4 measurement time of 1 h were assumed.
 5



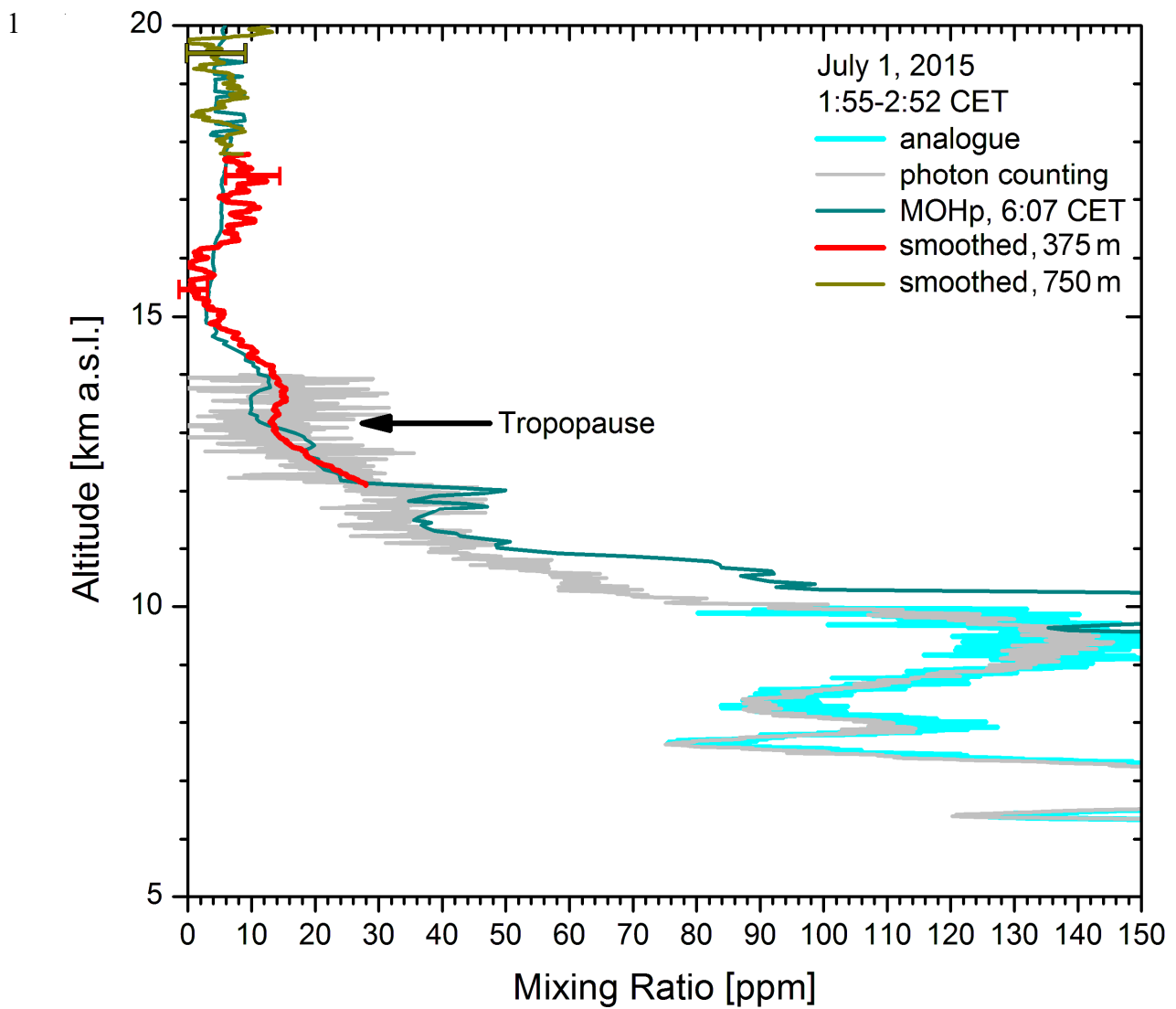
2 **Fig. 11.** Comparison of consecutive measurements of the Raman lidar and DIAL at UFS on 25 April, 2013: the
 3 sonde measurements at Munich (not shown) and Innsbruck strongly differ from those of the lidar systems. For
 4 comparison, we show the densities corresponding to 20 % RH as calculated from the Munich radiosonde.

5
 6



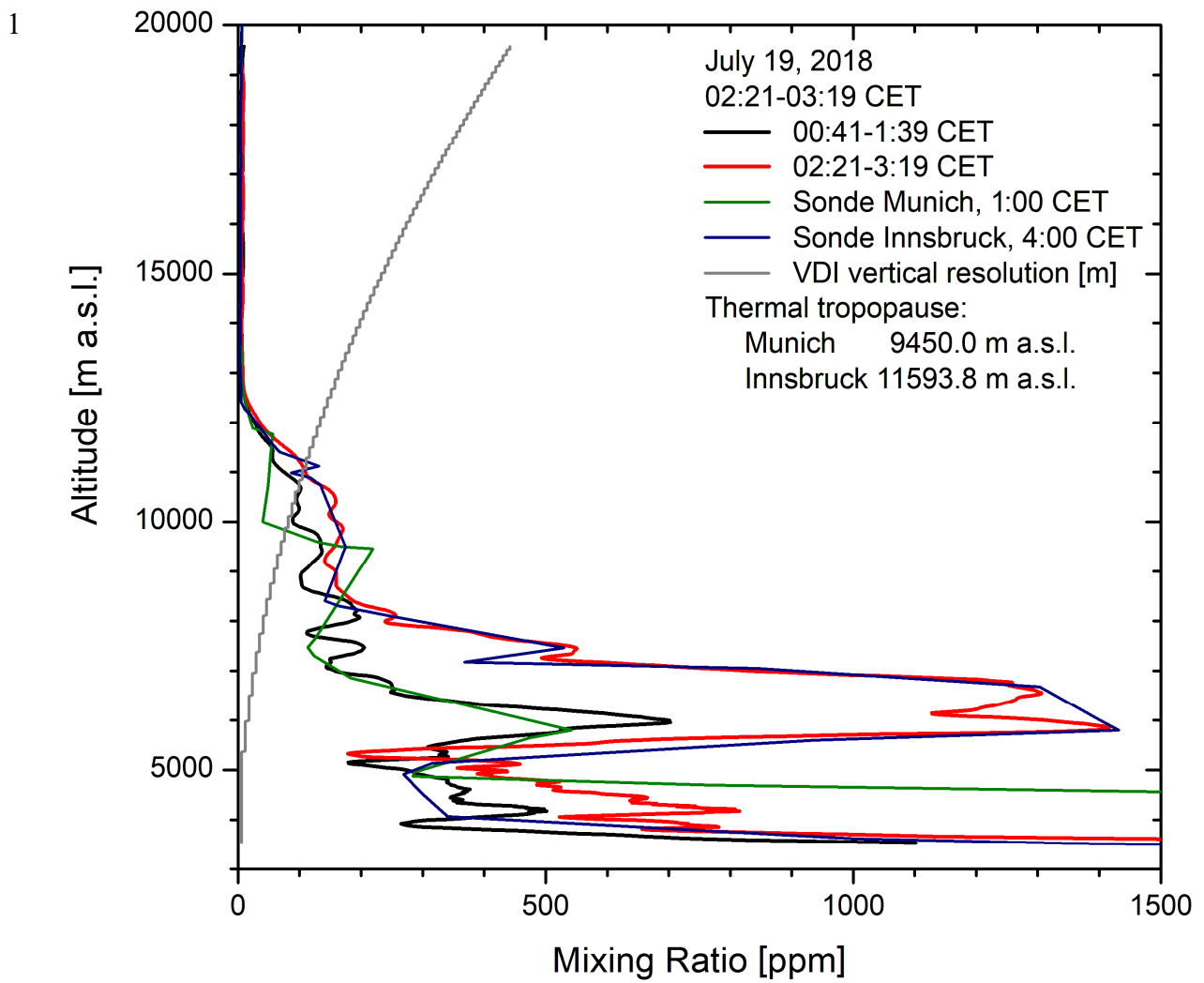
2 **Fig. 12.** 347-nm Raman backscatter signals as a function of the vertical distance above UFS, obtained during the
 3 first hours on 1 July, 2015. Despite a high noise level of about 12 counts (square root of signal) the averaged
 4 signal remains positive up to $r = 19.7$ km. The averaged signal covers six decades, the peak signal being roughly
 5 3 mV. The average laser pulse energy, 295 mJ, was low due to a contaminated cell window.

6
 7

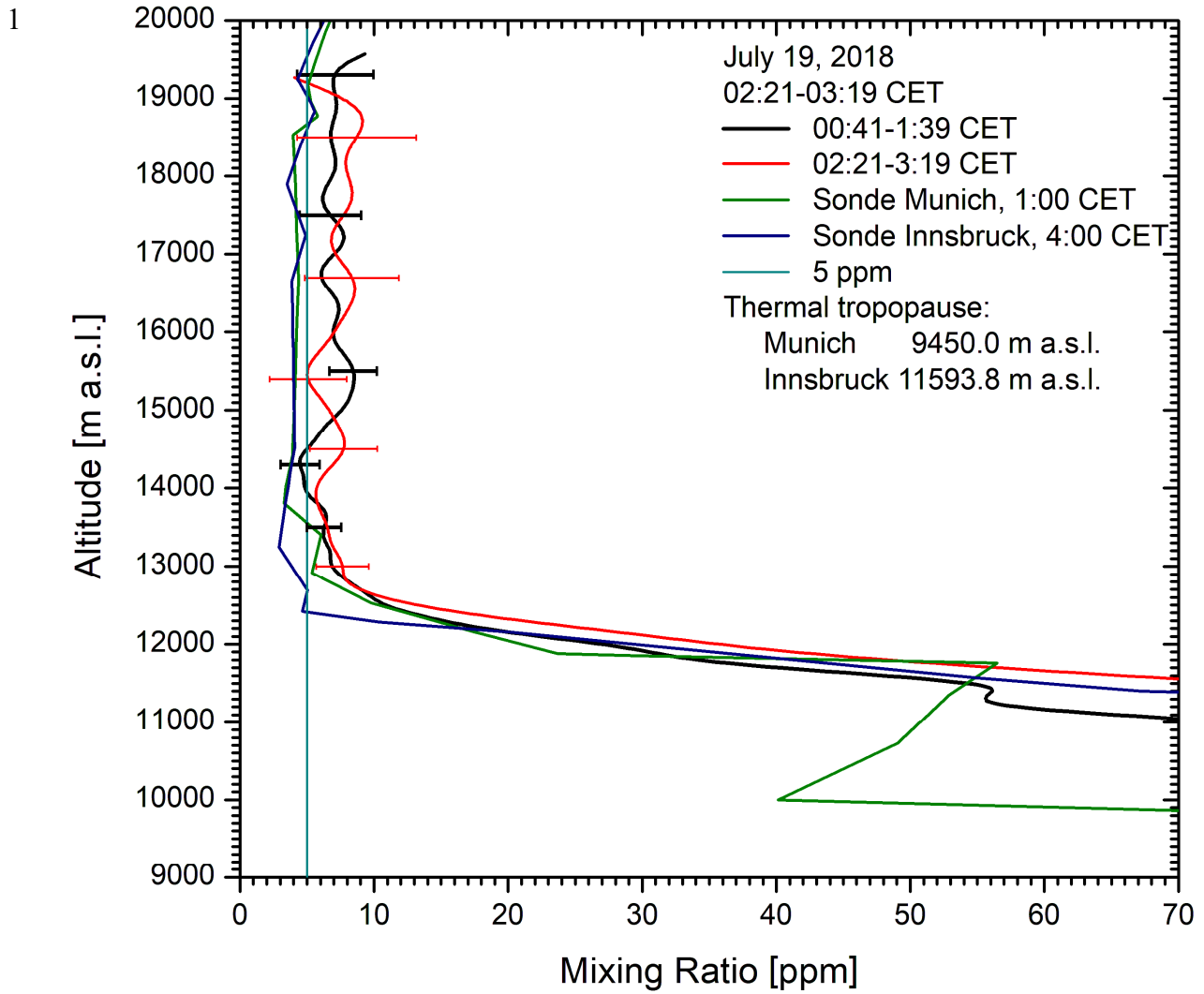


2 **Fig. 13.** Water-vapour mixing ratio obtained for the measurement in Fig. 15; the calibration is based on looking
 3 at zones of best agreement below 7 km between the sonde data for Munich (1 CET), Innsbruck (4 CET) and
 4 Hohenpeißenberg (6 CET). Just the Hohenpeißenberg (MOHp) results are displayed here because they agree best
 5 with the lidar values above 11 km. 51-pt and 101-pt arithmetic-means smoothing was applied to the mixing
 6 ratios derived from the photon-counting data at high altitudes, the corresponding VDI vertical resolutions are
 7 specified in the legend.

8

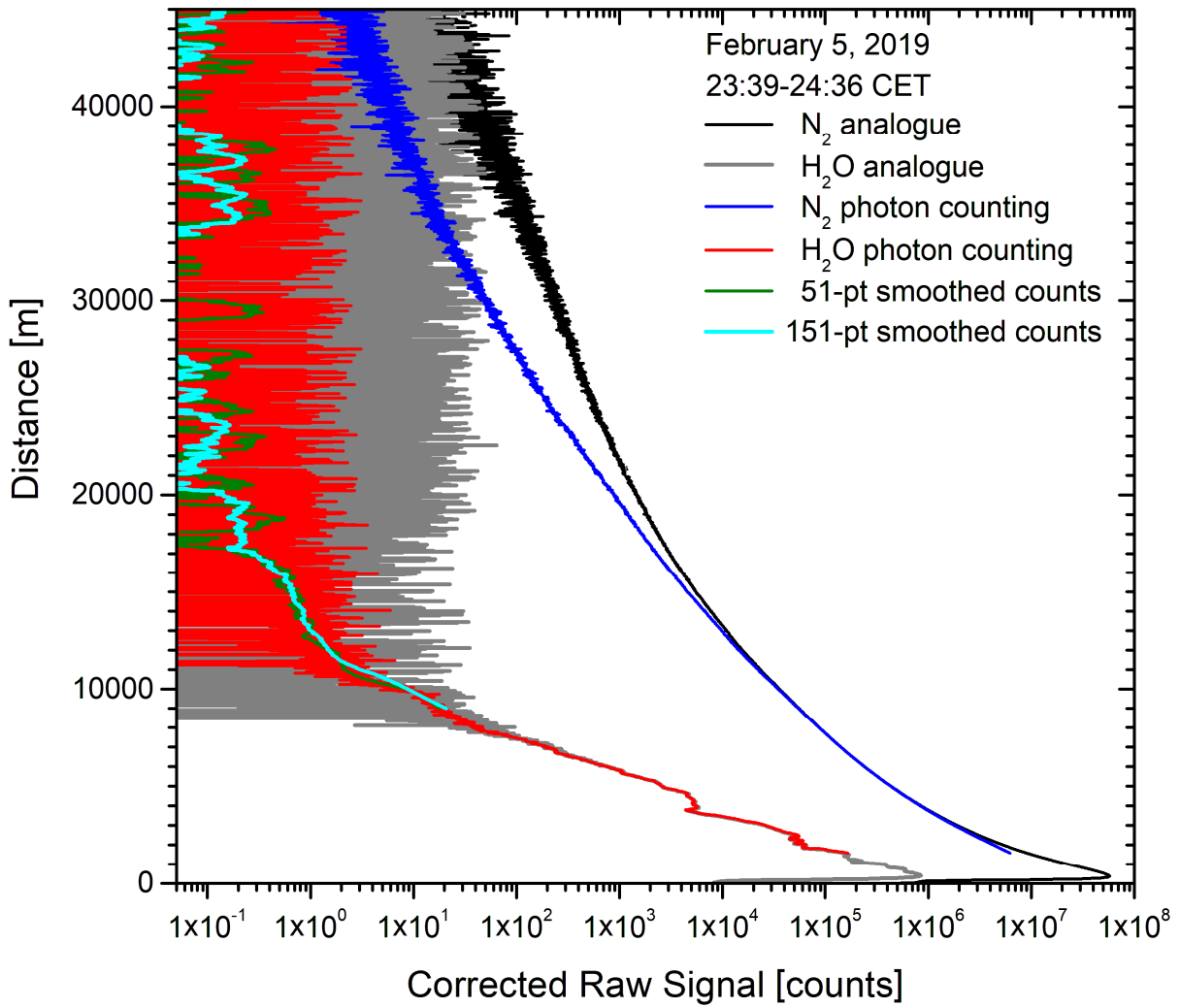


2 **Fig. 14.** Calibration of the measurements on 19 July 2018: The profile derived from the first measurement agrees
 3 better with the 1:00 CET sonde data from Munich. The mixing ratios for the second measurement almost
 4 coincides with those from the later sonde launch at the airport of Innsbruck. The average laser pulse energy was
 5 380 mJ (300 Hz).
 6



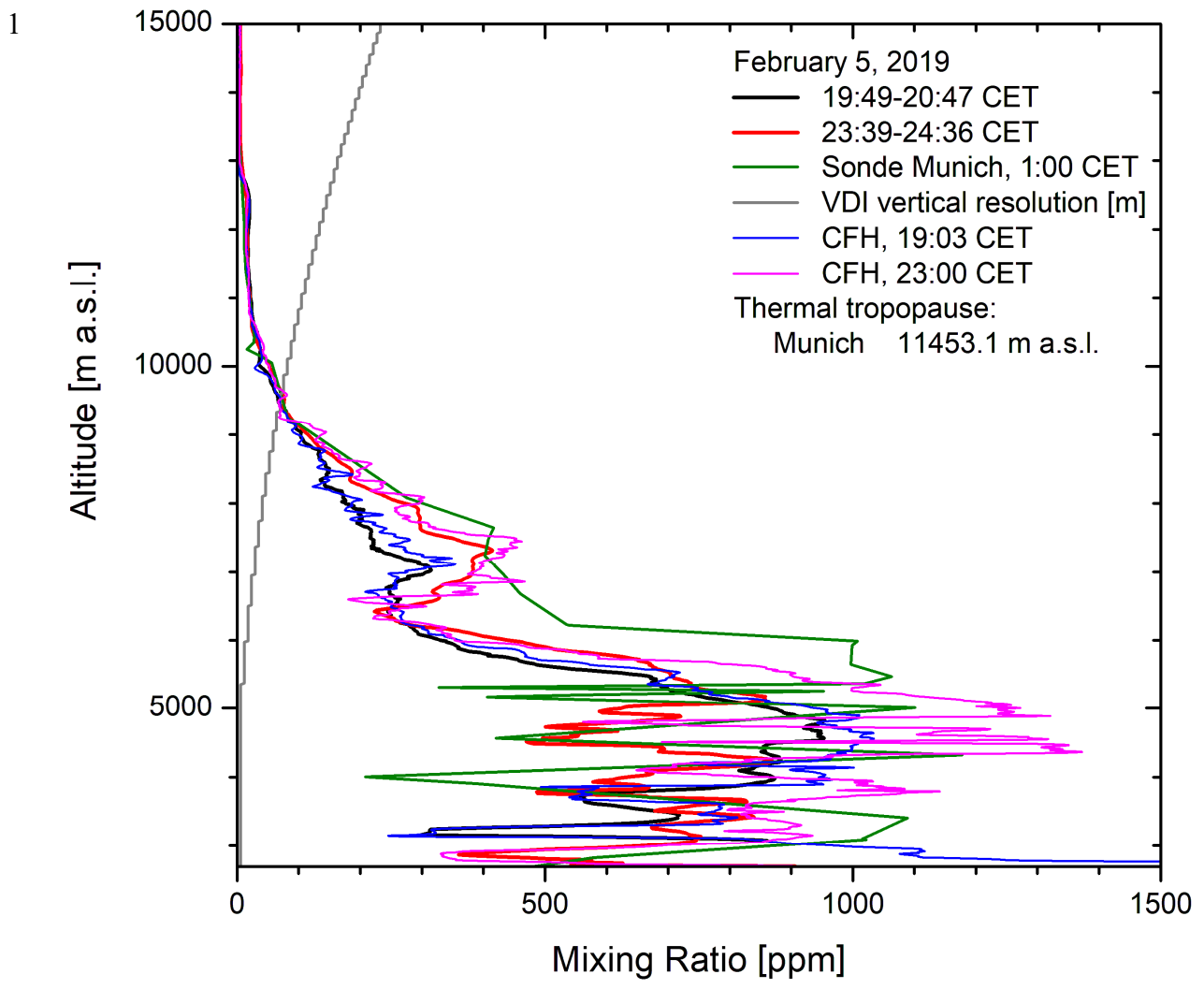
2 **Fig. 15.** Comparison of the two lidar measurements on 19 July, 2018, and the Innsbruck sonde on a zoomed
 3 scale: The lidar values agree well up to 18 km, ranging between 5 ppm and 12 ppm. The mixing ratio for the
 4 radiosondes (presumably RS41) is much lower than that for the lidar in the stratosphere.
 5

1

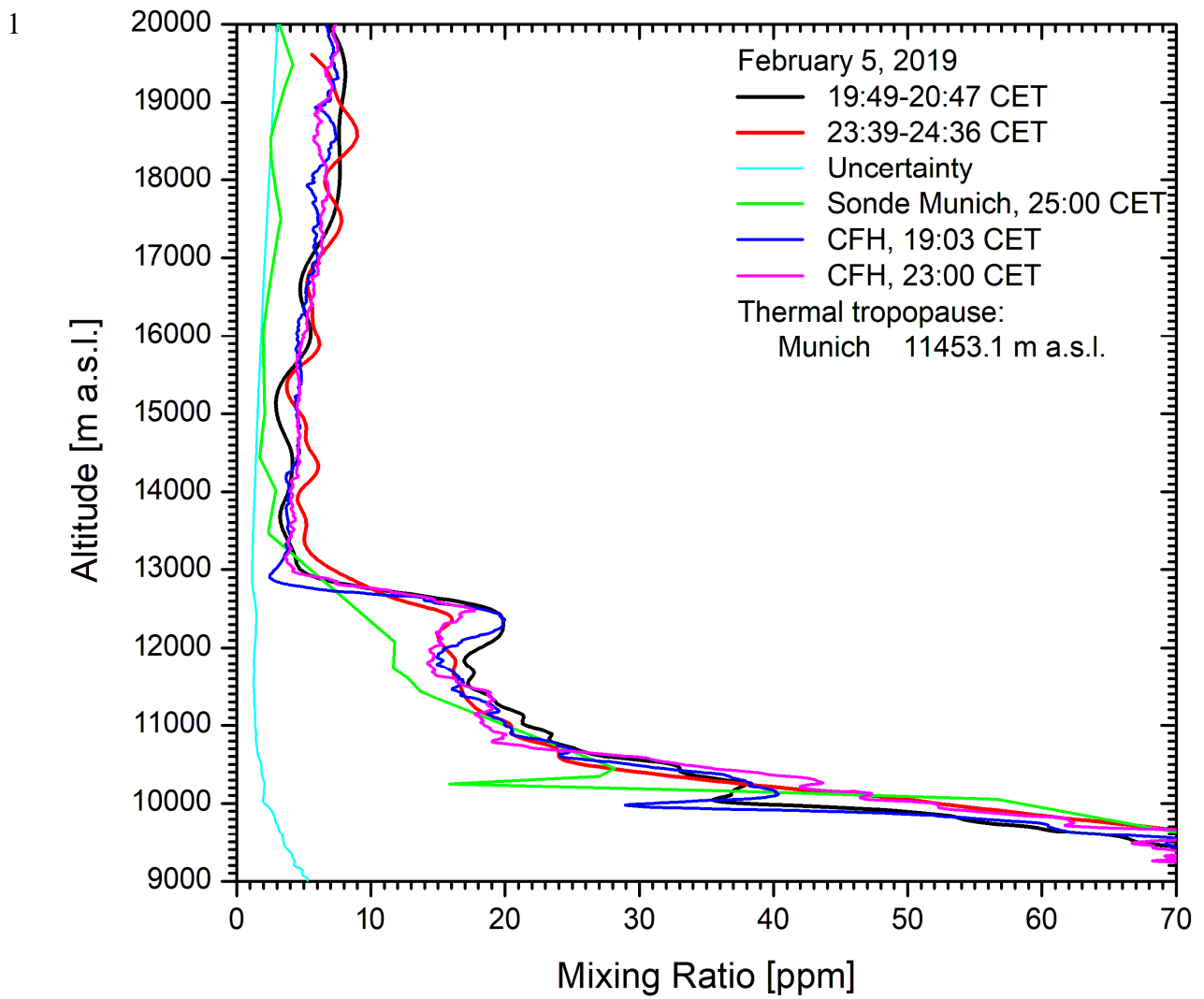


2 **Fig. 16.** Nitrogen and water-vapour backscatter signals on 5 February 2019 as a function of the vertical distance
3 above UFS; The H₂O backscatter profiles averaged over 151 7.5-m bins (i.e., raw data; VDI vertical resolution:
4 562.5 m) become noisy at about 17 km (19.7 km a.s.l.). The laser pulse energy was just 360 mJ (300 Hz).

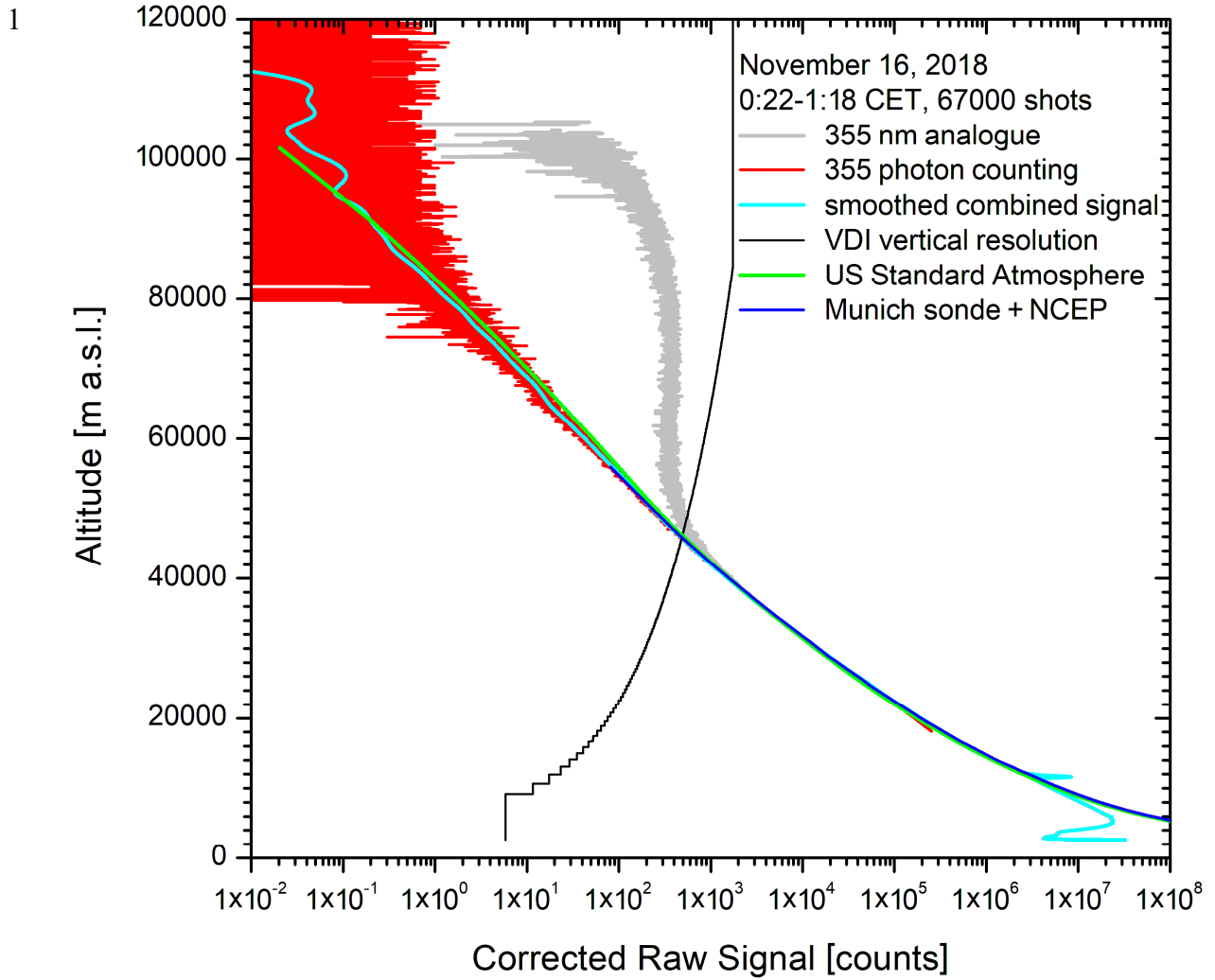
5
6
7
8
9



2 **Fig. 17.** Vertical distributions of water-vapour derived from two measurements of the Raman lidar on 5 February
 3 2019 together with those from the midnight Munich sonde and the CFH sensors; the CFH data in the upper
 4 troposphere were used for calibration.
 5



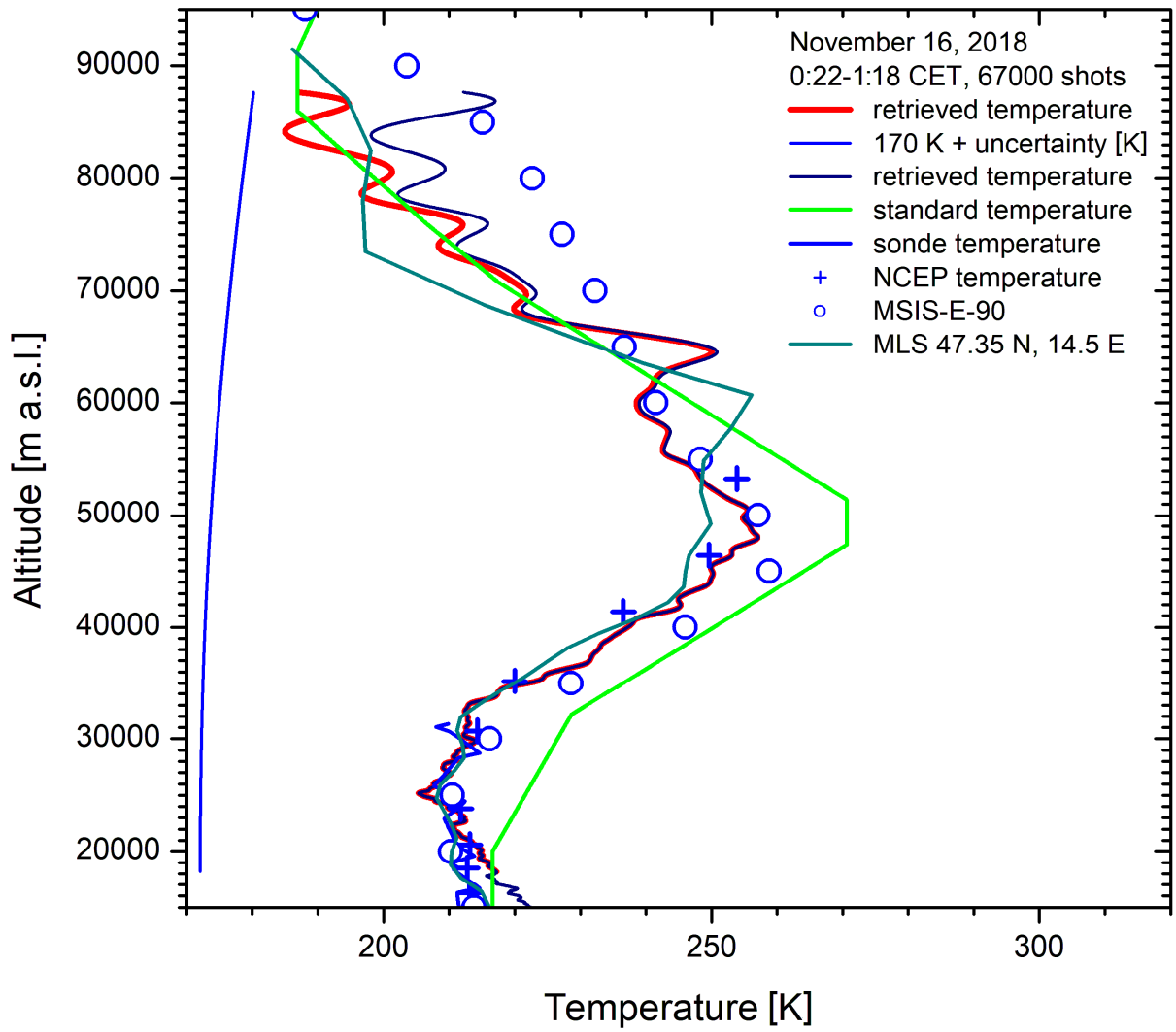
2 **Fig. 18.** Zoomed portion of Fig. 20: The agreement between lidar and CFH is satisfactory up to almost 20 km.
 3 Above this, the lidar values start wider excursions around the CFH mixing ratios.
 4
 5



2 **Fig. 19.** 355-nm backscatter coefficients for a 355-nm measurement on November 16, 2018 together with the
 3 smoothed combined analogue plus photon counting signal; the VDI vertical resolution of the smoothing
 4 procedure is given in metres. Simulated backscatter signals calculated from the U.S. Standard Atmosphere
 5 (1976) a combined radiosonde and NCEP profile are included for comparison.

6

1



2 **Fig. 20.** Temperature profile from the measurement in Fig. 21, in comparison with data from the Munich 1:00
3 CET radiosonde, NCEP (13:00 CET), the MSIS model and MLS; the temperatures were retrieved from the lidar
4 signal by initializing the temperature at about 87 km using both the U.S. Standard and the MSIS values. Both
5 retrievals converge to the same curve within 15-20 km from the top.